



HAL
open science

Normal Integration – Part II: New Insights

Yvain Quéau, Jean-Denis Durou, Jean-François Aujol

► **To cite this version:**

Yvain Quéau, Jean-Denis Durou, Jean-François Aujol. Normal Integration – Part II: New Insights. 2016. hal-01334351v1

HAL Id: hal-01334351

<https://hal.science/hal-01334351v1>

Preprint submitted on 20 Jun 2016 (v1), last revised 18 Sep 2017 (v3)

HAL is a multi-disciplinary open access archive for the deposit and dissemination of scientific research documents, whether they are published or not. The documents may come from teaching and research institutions in France or abroad, or from public or private research centers.

L'archive ouverte pluridisciplinaire **HAL**, est destinée au dépôt et à la diffusion de documents scientifiques de niveau recherche, publiés ou non, émanant des établissements d'enseignement et de recherche français ou étrangers, des laboratoires publics ou privés.

Normal Integration – Part II: New Insights

Yvain Quéau · Jean-Denis Durou · Jean-François Aujol

the date of receipt and acceptance should be inserted later

Abstract The need for an efficient method of integration of a dense normal field is inspired by several computer vision tasks, such as shape-from-shading, photometric stereo, deflectometry, etc. Our work is divided into two papers. In the first paper entitled *Part I: A Survey*, we have selected the most important properties that one may expect from any integration method. We have then reviewed most existing methods, according to the selected properties, and concluded that no method satisfies all of them. In the present paper entitled *Part II: New Insights*, we propose several variational methods which aim at filling this gap. We first introduce a new discretization for quadratic integration, which is designed to ensure both fast recovery and the ability to handle non-rectangular domains. Yet, with this solver, discontinuous surfaces can be handled only if the scene is a priori segmented into pieces without discontinuity. Inspired by edge-preserving methods from image processing (e.g., total variation and non-convex regularization, anisotropic diffusion and variational segmentation), we then introduce several discontinuity-preserving functionals. In view of the selected criteria, that inspired by the Mumford-Shah segmentation method is shown to be the best compromise.

Keywords 3D-reconstruction, integration, normal field, gradient field, photometric stereo, shape-from-shading.

Y. Quéau
IRIT, Université de Toulouse, France
E-mail: yvain.queau@enseiht.fr

J.-D. Durou
IRIT, Université de Toulouse, France

J.-F. Aujol
IMB, Université de Bordeaux, Talence, France
Institut Universitaire de France

1 Introduction

In this paper, we study several methods for numerical integration of a gradient field over a 2D grid. Our aim is to estimate the values of a function $z : \mathbb{R}^2 \rightarrow \mathbb{R}$, over a set $\Omega \subset \mathbb{R}^2$ where an estimate $\mathbf{g} = [p, q]^\top : \Omega \rightarrow \mathbb{R}^2$ of its gradient ∇z is available. Formally, we want to estimate values $z(u, v)$ satisfying the following equation in z :

$$\nabla z(u, v) = \underbrace{[p(u, v), q(u, v)]^\top}_{\mathbf{g}(u, v)}, \forall (u, v) \in \Omega \quad (1)$$

where $\nabla z(u, v)$ is the gradient of the unknown *depth map* z , $\mathbf{g} = [p, q]^\top$ is the data, i.e. an estimate of ∇z , and $\Omega \subset \mathbb{R}^2$ is the *reconstruction domain*.

1.1 Expected Properties of an Integration Method

In our survey paper [19], we have shown that an ideal numerical tool for solving equation (1) should satisfy the following properties, apart accuracy:

- $\mathcal{P}_{\text{Fast}}$: be as *fast* as possible;
- $\mathcal{P}_{\text{Robust}}$: be *robust* to a noisy gradient field;
- $\mathcal{P}_{\text{FreeB}}$: be able to handle a *free boundary*;
- $\mathcal{P}_{\text{Disc}}$: preserve the *depth discontinuities*;
- $\mathcal{P}_{\text{NoRect}}$: be able to work on a *non-rectangular domain* Ω ;
- $\mathcal{P}_{\text{NoPar}}$: have no *critical parameter* to tune.

We have also shown in [19] that no existing method simultaneously meets all these requirements. Building upon the conference papers [18, 20, 48], our aim in this second paper is to fill this gap, through the study of several variational formulations of the integration problem.

1.2 Variational Methods in Image Processing

In view of the $\mathcal{P}_{\text{Robust}}$ property, variational methods, which aim at estimating the surface by minimization of a well-chosen criterion, are particularly suited for the integration problem. Hence, we choose the variational framework as basis for the design of new methods. This choice is also motivated by the fact that the property which is the most difficult to ensure is probably $\mathcal{P}_{\text{Disc}}$. Numerous variational methods have been designed for edge-preserving image processing: such methods may thus be a natural source of inspiration for designing discontinuity-preserving integration methods.

For a comprehensive introduction to this literature, we refer the reader to [3] and to pioneering papers such as [10, 15, 35, 39]. Basically, the idea in edge-preserving image restoration is that edges need to be processed in a particular way. This is usually achieved by choosing an appropriate energy to minimize, formulating the inverse problem as the recovery of a restored image $z : \Omega \subset \mathbb{R}^2 \rightarrow \mathbb{R}$ minimizing the energy:

$$\mathcal{E}(z) = \mathcal{F}(z) + \mathcal{R}(z) \quad (2)$$

where:

- $\mathcal{F}(z)$ is a *fidelity* term penalizing the difference between a corrupted image z^0 and the restored image:

$$\mathcal{F}(z) = \iint_{(u,v) \in \Omega} \Phi(z(u,v) - z^0(u,v)) \, du \, dv \quad (3)$$

with Φ chosen accordingly to the type of corruption the original image z^0 is affected by. For instance, $\Phi_{L_2}(s) = s^2$ is the natural choice in the presence of additive, zero-mean, Gaussian noise, while $\Phi_{L_1}(s) = |s|$ can be used in the presence of bi-exponential (Laplacian) noise, which is a rather good model when outliers come into play (e.g., “salt & pepper” noise).

- $\mathcal{R}(z)$ is a *regularization* term, which usually penalizes the gradient of the restored image:

$$\mathcal{R}(z) = \iint_{(u,v) \in \Omega} \lambda(u,v) \Psi(\|\nabla z(u,v)\|) \, du \, dv \quad (4)$$

In (4), $\lambda \geq 0$ is a field of weights which control the respective influence of the fidelity and the regularization terms. It can be either manually tuned beforehand (if $\lambda(u,v) \equiv \lambda$, λ can be seen as a “hyperparameter”), or defined as a function of $\|\nabla z(u,v)\|$. The choice of Ψ must be made accordingly to a prior one has on the image smoothness. The *quadratic penalty* $\Psi_{L_2}(s) = s^2$ will produce “smooth” images,

while piecewise-constant images are obtained when choosing the *sparsity penalty* $\Psi_{L_0}(s) = 1 - \delta(s)$, with $\delta(s) = 1$ if $s = 0$ and $\delta(s) = 0$ otherwise. The latter approach preserves the edges, but the numerical resolution is much more difficult, since the regularization term is non-smooth and non-convex. Hence, several choices of regularizers “inbetween” the quadratic and the sparsity ones have been suggested. For instance, the infamous total variation (TV) regularizer is obtained by setting $\Psi(s) = |s|$. Efficient numerical methods exist for solving this non-smooth, yet convex, problem. Examples include primal-dual methods [12], augmented Lagrangian (ADMM, Bregman iterations) approaches [24], and forward-backward splittings [41]. The latter can also be adapted to the case where the regularizer Ψ is non-convex, but smooth [42]. Such non-convex regularization terms were shown to be particularly effective for edge-preserving image restoration [23, 37, 39]. Another strategy is to apply least-squares in a non-uniform manner. For instance, setting weights $\lambda(u,v)$ in (4) inversely proportional to $\|\nabla z(u,v)\|$ yields the “anisotropic diffusion” model by Perona and Malik [45]. The discontinuity points can also be automatically estimated and discarded, in the spirit of Mumford and Shah’s segmentation method [38].

1.3 Notations

Although we chose for simplicity to write the variational problems in a continuous form, we are overall interested in solving discrete problems. Two different discretization strategies exist. The first one consists in using variational calculus to derive the (continuous) necessary optimality condition, then discretize it by finite differences, and eventually solve the discretized optimality condition. The alternative method, inspired by the finite elements method, is to discretize the functional itself by finite differences, before solving the optimality condition associated to the discrete problem. As shown in [20], the latter approach eases the handling of the boundary of Ω , hence we use it as discretization strategy. The variational models hereafter will be presented using the continuous notations, because we find them more readable. The discrete notations will be used only when deriving the numerical resolution. Yet, to avoid confusion, we will use caligraphic letters for the continuous energies (e.g., \mathcal{E} , \mathcal{F} , \mathcal{R}), and capital letters for their discrete counterparts (e.g., E , F , R). With these conventions, it should be clear whether an optimization problem is discrete or continuous. Hence, we will use the same notation $\nabla z = [\partial_u z, \partial_v z]^\top$ in both cases, keeping in mind that this notation represents either the gradient of z or a finite differences approximation.

1.4 Proposed Variational Framework

In this work, we show how to adapt the aforementioned variational models, originally designed for image restoration, to the normal integration problem. Although both these inverse problems are formally very similar, they are somehow different, for the following reasons. 1) The concept of edges in an image to restore is replaced by those of depth discontinuities and kinks. 2) Contrarily to image processing functionals, our data consist in an estimate \mathbf{g} of the *gradient* of the unknown z , in lieu of a corrupted version z^0 of z . As a consequence, the fidelity term $\mathcal{F}(z)$ will apply to the difference between ∇z and \mathbf{g} , and it is the choice of this term which will or not allow depth discontinuities. 3) Regularization terms are optional here: all the methods we discuss basically work even with $\mathcal{R}(z) \equiv 0$, but we may use this regularization term to allow introducing, if available, a prior on the surface (e.g., user-defined control points [31, 34] or a rough depth estimate obtained using a low-resolution depth sensor [33]). As stated in our survey paper [19], such feature “is appreciable, although not required”.

We will discuss methods seeking the unknown depth z as the minimizer of an energy $\mathcal{E}(z) = \mathcal{F}(z) + \mathcal{R}(z)$ in the form (2), but with different choices for $\mathcal{F}(z)$ and $\mathcal{R}(z)$:

- $\mathcal{F}(z)$ now represents a fidelity term penalizing the difference between the gradient of the recovered depth map z and the datum \mathbf{g} :

$$\mathcal{F}(z) = \iint_{(u,v) \in \Omega} \Phi(\|\nabla z(u,v) - \mathbf{g}(u,v)\|) \, du \, dv \quad (5)$$

- $\mathcal{R}(z)$ now represents prior knowledge of the depth:

$$\mathcal{R}(z) = \iint_{(u,v) \in \Omega} \lambda(u,v) [z(u,v) - z^0(u,v)]^2 \quad (6)$$

where z^0 is the prior, and $\lambda(u,v) \geq 0$ is a user-defined, spatially-varying, regularization weight. Let us remark that we consider only quadratic regularization: studying more robust regularization terms (e.g., L^1 norm) is left as perspective. The purpose of this prior term is to avoid numerical instabilities which may arise when considering solely the fidelity term (5): since this fidelity term depends only on ∇z , and not on z , the minimizer of (5) can be estimated only up to an additive ambiguity $z(u,v) = z(u,v) + k$, where k is an integration constant. As discussed hereafter, the regularization term also enables the introduction of a priori knowledge of the surface.

1.5 Choosing λ and z^0

A first situation where the regularization term may have other purposes than ensuring stability is when one would like to impose one or several control points on the surface [31, 34]. This can be achieved very simply within the proposed variational framework, by setting $\lambda(u,v) \equiv 0$ everywhere, except on the control points locations (u,v) where a high value for $\lambda(u,v)$ must be set and the value $z^0(u,v)$ is fixed.

The second typical situation is when, given both a coarse depth estimate and an accurate normal estimate, one would like to “merge” them in order to create a high-quality depth map. Such a problem arises, for instance, when refining the depth map of an RGB-D sensor (e.g., the Kinect) by means of shape-from-shading [43], photometric stereo [26] or shape-from-polarization [33]. In such cases, we may set z^0 to the coarse depth map, and visually select the value of $\lambda(u,v) \equiv \lambda$ that offers the “best” 3D-reconstruction. Let us note that our framework allows using non-uniform weights, which can be useful in order to lower the influence of outliers in the coarse depth map [26].

Eventually, in the absence of such priors, we will use the regularization term only to fix the integration constant: this is easily achieved by setting an arbitrary prior (e.g., $z^0(u,v) \equiv 0$), along with a small value for λ (typically, $\lambda(u,v) \equiv \lambda = 10^{-6}$).

1.6 Structure of the Paper

We will study in the next sections several choices for the fidelity term $\mathcal{F}(z)$ defined in (5), which all enforce the $\mathcal{P}_{\text{Robust}}$ property. Whatever this choice, we will see that a proper discretization of the energy-minimization framework allows us to naturally handle both $\mathcal{P}_{\text{FreeB}}$ and $\mathcal{P}_{\text{NoRect}}$. Since it is difficult to design a method which handles both $\mathcal{P}_{\text{Fast}}$ and $\mathcal{P}_{\text{Disc}}$, the rest of this paper is split into two parts. We first consider in section 2 the case of *smooth* surfaces, and introduce for this purpose a new quadratic integration method which is both very fast and parameter-free. With this method, which extends that proposed in [20], all properties except $\mathcal{P}_{\text{Disc}}$ are enforced. On the other hand, when the surface to recover is only piecewise-smooth, discontinuities and kinks have to be properly handled. We introduce in section 3 several new functionals, some of them having been initially proposed in [18, 48], which allow the recovery of these sharp features. Although the $\mathcal{P}_{\text{Disc}}$ property is enforced using such methods, we will see that numerical methods become slower, and that one or several parameters need to be tuned.

2 Smooth Surfaces

We first tackle the problem of recovering a “smooth” depth map z from a noisy estimate \mathbf{g} of ∇z . To this end, we consider the quadratic variational problem:

$$\min_z \iint_{(u,v) \in \Omega} \|\nabla z(u,v) - \mathbf{g}(u,v)\|^2 + \lambda(u,v) [z(u,v) - z^0(u,v)]^2 du dv \quad (7)$$

which admits a unique solution $z \in W^{1,2}(\Omega)$. Our purpose in this section is to introduce efficient numerical schemes for approximating this solution.

If the depth map z is further assumed to be twice differentiable, the necessary optimality condition associated to the continuous optimization problem (7) (Euler-Lagrange equation) can be derived. This condition is a linear PDE in z : discretizing it using finite differences yields a linear system of equations in the values $z(u,v)$ of the depth map. This system can be efficiently solved by means of the conjugate gradient algorithm, provided that appropriate preconditioning and initialization are used [9]. Yet, as discussed by Harker and O’Leary in [27], providing a consistent discretization on the boundary of Ω is not straightforward, which may be a source of bias. This is even more true when dealing with non-rectangular domains Ω (cf. subsection 2.4). Hence, following the advice in [27], and earlier work in [20,30], we consider a different route, based on the discretization of the functional itself.

2.1 Discretizing the Functional

Instead of a continuous gradient field $\mathbf{g} : \Omega \rightarrow \mathbb{R}^2$ over an open set Ω , we are actually given a finite set of values $\{\mathbf{g}_{u,v} = [p_{u,v}, q_{u,v}]^\top, (u,v) \in \Omega\}$, where the (u,v) represent the *pixels* of the discrete part Ω of a 2D grid¹. Solving the discrete integration problem requires estimating a finite set of values, i.e. the $|\Omega|$ unknown depth values $z_{u,v}$, $(u,v) \in \Omega$ ($|\cdot|$ denotes the cardinality), which are stacked columnwise in a vector $\mathbf{z} \in \mathbb{R}^{|\Omega|}$.

As discussed in our survey paper [19], assuming that the noise contained in \mathbf{g} is Gaussian-distributed may not be very meaningful in 3D-reconstruction applications such as photometric stereo [55], since the assumption on the noise should rather be formulated on the images. As a consequence, the least-squares variational model (7) may not yield optimal results. This issue will be discussed in more detail in subsection 3.4, where we introduce the maximum-likelihood estimator for z , assuming Gaussian distribution of the noise in the images.

¹ To ease the comparison between the variational and the discrete problems, we will use the same notation Ω for both the open set of \mathbb{R}^2 and the discrete subset of the grid.

For now, let us use a Gaussian approximation for the noise contained in \mathbf{g} , i.e., let us assume in the rest of this section that each datum $\mathbf{g}_{u,v}$, $(u,v) \in \Omega$, is equal to the gradient $\nabla z(u,v)$ of the unknown depth map z , taken at point (u,v) , up to a zero-mean additive, homoskedastic (same variance at each location (u,v)), Gaussian noise:

$$\mathbf{g}_{u,v} = \nabla z(u,v) + \boldsymbol{\epsilon}(u,v) \quad (8)$$

where $\boldsymbol{\epsilon}(u,v) \sim \mathcal{N}\left([0,0]^\top, \begin{bmatrix} \sigma^2 & 0 \\ 0 & \sigma^2 \end{bmatrix}\right)$ and σ is unknown².

Now, we need to give a discrete interpretation of the gradient operator in (8), through finite differences.

In order to obtain a second-order accurate discretization, we combine forward and backward first-order finite differences, i.e. we consider that each measure of the gradient $\mathbf{g}_{u,v} = [p_{u,v}, q_{u,v}]^\top$ provides us with up to four independent and identically distributed (i.i.d.) statistical observations, depending on the neighborhood of (u,v) . Indeed, its first component $p_{u,v}$ can be understood either in terms of both forward or backward finite differences (when both the bottom and the top neighbors are inside Ω), by one of both these discretizations (only one neighbor inside Ω), or by none of these finite differences (no neighbor inside Ω). Formally, we model the p -observations in the following way:

$$p_{u,v} = \overbrace{z_{u+1,v} - z_{u,v}}^{\partial_u^+ z_{u,v}} + \epsilon_u^+(u,v), \quad \forall (u,v) \in \underbrace{\{(u,v) \in \Omega \mid (u+1,v) \in \Omega\}}_{\Omega_u^+} \quad (9)$$

$$p_{u,v} = \overbrace{z_{u,v} - z_{u-1,v}}^{\partial_u^- z_{u,v}} + \epsilon_u^-(u,v), \quad \forall (u,v) \in \underbrace{\{(u,v) \in \Omega \mid (u-1,v) \in \Omega\}}_{\Omega_u^-} \quad (10)$$

where $\epsilon_u^{+/-} \sim \mathcal{N}(0, \sigma^2)$. Hence, rather than considering that we are given $|\Omega|$ observations p , our discretization handles these data as $|\Omega_u^+| + |\Omega_u^-|$ observations, some of them being interpreted in terms of forward differences, some in terms of backward differences, some in terms of both forward and backward differences, the points without any neighbor in the u -direction being excluded.

This discretization is different from that proposed by Horn and Brooks [30] (which is discussed in detail in our survey paper [19]), who consider only forward finite differences, yet replace the values $p(u,v)$ by their forward mean values $\frac{1}{2}(p(u,v) + p(u+1,v))$, in order

² The assumptions of equal variance σ^2 for both components and of a diagonal covariance matrix are introduced only for consistency with the least-squares problem (7). They are discussed with more care in section 3.4.

to reach a second-order accurate discretization. We believe that it is clearer to keep the original values $p(u, v)$, while ensuring discretization accuracy by combination of forward and backward finite differences.

Symmetrically, the second component q of \mathbf{g} corresponds either to two, one or zero observations:

$$q_{u,v} = \overbrace{z_{u,v+1} - z_{u,v}}^{\partial_v^+ z_{u,v}} + \epsilon_v^+(u, v),$$

$$\forall (u, v) \in \underbrace{\{(u, v) \in \Omega \mid (u, v+1) \in \Omega\}}_{\Omega_v^+} \quad (11)$$

$$q_{u,v} = \overbrace{z_{u,v} - z_{u,v-1}}^{\partial_v^- z_{u,v}} + \epsilon_v^-(u, v),$$

$$\forall (u, v) \in \underbrace{\{(u, v) \in \Omega \mid (u, v-1) \in \Omega\}}_{\Omega_v^-} \quad (12)$$

where $\epsilon_v^{+/-} \sim \mathcal{N}(0, \sigma^2)$. Given the Gaussianity of the noises $\epsilon_{u/v}^{+/-}$, their independence, and the fact that they all share the same standard deviation σ and mean 0, the joint likelihood of the observed gradients $\{\mathbf{g}_{u,v}\}_{(u,v)}$ is:

$$L(\{\mathbf{g}_{u,v}, (u, v) \in \Omega\} \mid \{z_{u,v}, (u, v) \in \Omega\})$$

$$= \prod_{(u,v) \in \Omega_u^+} \frac{1}{\sqrt{2\pi\sigma^2}} \exp\left\{-\frac{[\partial_u^+ z_{u,v} - p_{u,v}]^2}{2\sigma^2}\right\}$$

$$\times \prod_{(u,v) \in \Omega_u^-} \frac{1}{\sqrt{2\pi\sigma^2}} \exp\left\{-\frac{[\partial_u^- z_{u,v} - p_{u,v}]^2}{2\sigma^2}\right\}$$

$$\times \prod_{(u,v) \in \Omega_v^+} \frac{1}{\sqrt{2\pi\sigma^2}} \exp\left\{-\frac{[\partial_v^+ z_{u,v} - q_{u,v}]^2}{2\sigma^2}\right\}$$

$$\times \prod_{(u,v) \in \Omega_v^-} \frac{1}{\sqrt{2\pi\sigma^2}} \exp\left\{-\frac{[\partial_v^- z_{u,v} - q_{u,v}]^2}{2\sigma^2}\right\} \quad (13)$$

and hence the maximum-likelihood estimate for the depth values is obtained by minimizing:

$$F_{L_2}(\mathbf{z}) = \frac{1}{2} \left(\sum_{(u,v) \in \Omega_u^+} [\partial_u^+ z_{u,v} - p_{u,v}]^2 \right.$$

$$\left. + \sum_{(u,v) \in \Omega_u^-} [\partial_u^- z_{u,v} - p_{u,v}]^2 \right)$$

$$+ \frac{1}{2} \left(\sum_{(u,v) \in \Omega_v^+} [\partial_v^+ z_{u,v} - q_{u,v}]^2 \right.$$

$$\left. + \sum_{(u,v) \in \Omega_v^-} [\partial_v^- z_{u,v} - q_{u,v}]^2 \right) \quad (14)$$

where the $\frac{1}{2}$ coefficients are meant to ease the continuous interpretation: the integral of the fidelity term in (7)

is approximated by $F_{L_2}(\mathbf{z})$, expressed in (14) as the mean of the forward and the backward discretizations.

To obtain a more concise representation of this fidelity term, let us stack the data in two vectors $\mathbf{p} \in \mathbb{R}^{|\Omega|}$ and $\mathbf{q} \in \mathbb{R}^{|\Omega|}$. In addition, let us introduce four $|\Omega| \times |\Omega|$, bi-diagonal, differentiation matrices \mathbf{D}_u^+ , \mathbf{D}_u^- , \mathbf{D}_v^+ and \mathbf{D}_v^- , associated with the finite differences operators $\partial_{u/v}^{+/-}$. For instance, the i -th line of \mathbf{D}_u^+ reads:

$$(\mathbf{D}_u^+)_{i,\cdot} =$$

$$\begin{cases} [0, \dots, 0, \underbrace{-1}_{\text{Position } i}, \underbrace{1}_{\text{Position } i+1}, 0, \dots, 0] & \text{if } m(i) \in \Omega_u^+ \\ \mathbf{0}^\top & \text{otherwise} \end{cases} \quad (15)$$

where we denote :

$$m : \{1, \dots, |\Omega|\} \rightarrow \Omega$$

$$i \mapsto m(i) = (u, v) \quad (16)$$

the mapping associating linear indices i with the pixel coordinates (u, v) .

Once these matrices are defined, (14) is equal to:

$$F_{L_2}(\mathbf{z}) = \frac{1}{2} \left(\|\mathbf{D}_u^+ \mathbf{z} - \mathbf{p}\|^2 + \|\mathbf{D}_u^- \mathbf{z} - \mathbf{p}\|^2 \right)$$

$$+ \frac{1}{2} \left(\|\mathbf{D}_v^+ \mathbf{z} - \mathbf{q}\|^2 + \|\mathbf{D}_v^- \mathbf{z} - \mathbf{q}\|^2 \right)$$

$$- \frac{1}{2} \left(\sum_{(u,v) \in \Omega \setminus \Omega_u^+} p_{u,v}^2 + \sum_{(u,v) \in \Omega \setminus \Omega_u^-} p_{u,v}^2 \right)$$

$$- \frac{1}{2} \left(\sum_{(u,v) \in \Omega \setminus \Omega_v^+} q_{u,v}^2 + \sum_{(u,v) \in \Omega \setminus \Omega_v^-} q_{u,v}^2 \right) \quad (17)$$

The terms in both the last rows of (17) being independent from the z -values, they do not influence the actual minimization and will thus be omitted from now on.

The regularization term (6) is discretized as:

$$R(\mathbf{z}) = \sum_{(u,v) \in \Omega} \lambda_{u,v} [z_{u,v} - z_{u,v}^0]^2 = \|\mathbf{A}(\mathbf{z} - \mathbf{z}^0)\|^2 \quad (18)$$

with \mathbf{A} a $|\Omega| \times |\Omega|$ diagonal matrix containing the values $\sqrt{\lambda_{u,v}}$, $(u, v) \in \Omega$.

Putting it altogether, our integration method for recovering smooth surfaces reads as the minimization of the discrete functional:

$$E_{L_2}(\mathbf{z}) = \frac{1}{2} \left(\|\mathbf{D}_u^+ \mathbf{z} - \mathbf{p}\|^2 + \|\mathbf{D}_u^- \mathbf{z} - \mathbf{p}\|^2 \right)$$

$$+ \frac{1}{2} \left(\|\mathbf{D}_v^+ \mathbf{z} - \mathbf{q}\|^2 + \|\mathbf{D}_v^- \mathbf{z} - \mathbf{q}\|^2 \right)$$

$$+ \|\mathbf{A}(\mathbf{z} - \mathbf{z}^0)\|^2 \quad (19)$$

2.2 Numerical Resolution

The optimality condition associated with the discrete functional (19) is a linear equation in \mathbf{z} :

$$\mathbf{A}\mathbf{z} = \mathbf{b} \quad (20)$$

where \mathbf{A} is a $|\Omega| \times |\Omega|$ symmetric matrix³:

$$\mathbf{A} = \frac{1}{2} \overbrace{\left[\mathbf{D}_u^{+\top} \mathbf{D}_u^+ + \mathbf{D}_u^{-\top} \mathbf{D}_u^- + \mathbf{D}_v^{+\top} \mathbf{D}_v^+ + \mathbf{D}_v^{-\top} \mathbf{D}_v^- \right]}^{\mathbf{L}} + \mathbf{A}^2 \quad (21)$$

and \mathbf{b} is a $|\Omega| \times 1$ vector:

$$\mathbf{b} = \frac{1}{2} \overbrace{\left[\mathbf{D}_u^{+\top} + \mathbf{D}_u^{-\top} \right]}^{\mathbf{D}_u} \mathbf{p} + \frac{1}{2} \overbrace{\left[\mathbf{D}_v^{+\top} + \mathbf{D}_v^{-\top} \right]}^{\mathbf{D}_v} \mathbf{q} + \mathbf{A}^2 \mathbf{z}^0 \quad (22)$$

The matrix \mathbf{A} is very sparse: it contains at most five non-zero entries per row. In addition, it is diagonal dominant: if $(\mathbf{A})_{i,i} = \mathbf{0}$, the value $(\mathbf{A})_{i,i}$ of a diagonal entry is equal to the opposite of the sum of the other entries $(\mathbf{A})_{i,j}$, $i \neq j$, from the same row i . It becomes strictly superior as soon as $(\mathbf{A})_{i,i}$ is strictly positive. Let us also remark that, when Ω describes a rectangular domain and the regularization weights are uniform ($\lambda(u, v) \equiv \lambda$), \mathbf{A} is a Toeplitz matrix. Yet, this structure is lost in the general case where it can only be said that \mathbf{A} is a sparse, symmetric, diagonal dominant (SDD) matrix with at most $5|\Omega|$ non-zero elements. It is positive semi-definite when $\mathbf{A} = \mathbf{0}$, and positive definite as soon as one of the $\lambda_{u,v}$ is non-zero.

System (20) can be solved by means of the conjugate gradient algorithm. Initialization will not influence the actual solution, but it may influence the number of iterations required to reach convergence. In our experiments, we used z^0 as initial guess, yet more elaborate initialization strategies may yield faster convergence [9]. To ensure $\mathcal{P}_{\text{Fast}}$, we used the multigrid preconditioning technique [36]. This bounds the computational complexity required to reach a ϵ relative accuracy⁴ by:

$$O(5|\Omega| \log |\Omega| \log(1/\epsilon)) \quad (23)$$

which is inbetween the complexities of the approaches based on Sylvester equations [27] (complexity $O(|\Omega|^{1.5})$) and on FFT [21] / DCT [53] ($O(|\Omega| \log(|\Omega|))$). On the other hand, these competing methods explicitly require that Ω is rectangular, while ours does not.

³ \mathbf{A} and \mathbf{b} are purposely divided by two in order to ease the continuous interpretation of subsection 2.3.

⁴ In our experiments, the threshold of the stopping criterion is set to $\epsilon = 10^{-4}$.

By construction, our integration method consisting in minimizing (19) satisfies the $\mathcal{P}_{\text{Robust}}$ property (it is the maximum-likelihood estimate in the presence of zero-mean Gaussian noise). The discretization we introduced does not assume any particular shape for Ω , neither treats the boundary in a specific manner, hence $\mathcal{P}_{\text{FreeB}}$ and $\mathcal{P}_{\text{NoRect}}$ are also satisfied. We also showed that $\mathcal{P}_{\text{Fast}}$ could be satisfied, using a resolution method based on the preconditioned conjugate gradient algorithm. Eventually, let us recall that tuning λ and/or manually fixing the values of the prior z_0 is necessary only to introduce a prior, but not in general. Hence, $\mathcal{P}_{\text{NoPar}}$ is also enforced. In conclusion, our integration method for smooth surfaces satisfies all the selected properties, except $\mathcal{P}_{\text{Disc}}$. Let us now provide additional remarks on the connections between the proposed discrete approach and a fully variational one.

2.3 Continuous Interpretation

One can remark that system (20) is nothing else than a discrete analogue of the Euler-Lagrange equation associated with the continuous functional (7). This optimality condition reads:

$$-\Delta z + \lambda z = -\nabla \cdot \mathbf{g} + \lambda z^0 \quad \text{over } \Omega \quad (24)$$

$$(\nabla z - \mathbf{g}) \cdot \boldsymbol{\eta} = 0 \quad \text{over } \partial\Omega \quad (25)$$

with $\boldsymbol{\eta}$ a normal vector to the boundary $\partial\Omega$ of Ω , Δ the Laplacian operator, and $\nabla \cdot$ the divergence operator.

Indeed, system (20) reads:

$$\underbrace{\mathbf{L}\mathbf{z}}_{\approx -\Delta z} + \underbrace{\mathbf{A}^2 \mathbf{z}}_{\approx \lambda z} = \underbrace{\mathbf{D}_u \mathbf{p} + \mathbf{D}_v \mathbf{q}}_{\approx -\nabla \cdot \mathbf{g}} + \underbrace{\mathbf{A}^2 \mathbf{z}^0}_{\approx \lambda z^0} \quad (26)$$

where the matrix-vector products are easily interpreted in terms of the differential operators in the continuous formula (24). One major advantage when reasoning from the beginning in the discrete setting is that one does not need to find out how to discretize the *natural*⁵ boundary condition (25), which was already emphasized in [20, 27]. Yet, the identifications in (26) show that both the discrete and continuous approaches are equivalent, provided that an appropriate discretization of the continuous optimality condition is used. It is thus possible to derive $O(5|\Omega| \log |\Omega| \log(1/\epsilon))$ algorithms based on the discretization of the Euler-Lagrange equation, contrarily to what is stated in [27]. The real drawback of such approaches does not lie in complexity, but in the difficult discretization of the boundary condition. This is further explored in the next subsection.

⁵ As stated in [27], homogeneous Neumann conditions of the type $\nabla z \cdot \boldsymbol{\eta} = 0$, used e.g. in [1], should be avoided.

2.4 Example

To clarify the proposed discretization of the integration problem, let us consider a non-rectangular domain Ω inside a 3×3 grid, like the one depicted in figure 1.

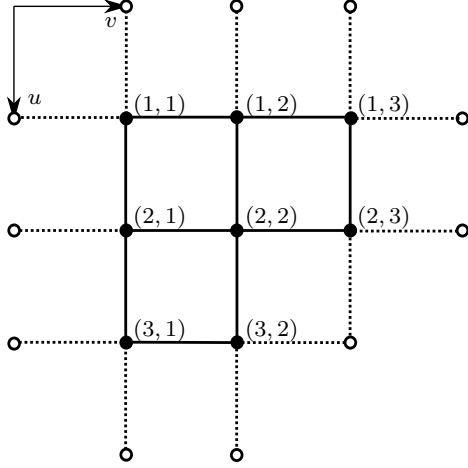


Fig. 1 Example of non-rectangular domain Ω (solid dots) inside a 3×3 grid. When invoking the continuous optimality condition, the discrete approximations of the Laplacian and the divergence near the boundary involve several points inside $\partial\Omega$ (circles) for which no data is available. First-order approximation of the *natural* boundary condition (25) is thus required. Relying only on discrete optimization simplifies a lot the boundary handling.

The vectorized unknown depth \mathbf{z} and the vectorized components \mathbf{p} and \mathbf{q} of the gradient write in this case:

$$\mathbf{z} = \begin{bmatrix} z_{1,1} \\ z_{2,1} \\ z_{3,1} \\ z_{1,2} \\ z_{2,2} \\ z_{3,2} \\ z_{1,3} \\ z_{2,3} \end{bmatrix} \quad \mathbf{p} = \begin{bmatrix} p_{1,1} \\ p_{2,1} \\ p_{3,1} \\ p_{1,2} \\ p_{2,2} \\ p_{3,2} \\ p_{1,3} \\ p_{2,3} \end{bmatrix} \quad \mathbf{q} = \begin{bmatrix} q_{1,1} \\ q_{2,1} \\ q_{3,1} \\ q_{1,2} \\ q_{2,2} \\ q_{3,2} \\ q_{1,3} \\ q_{2,3} \end{bmatrix} \quad (27)$$

The sets $\Omega_{u/v}^{+/-}$ all contain five pixels:

$$\Omega_u^+ = \{(1,1), (2,1), (1,2), (2,2), (1,3)\} \quad (28)$$

$$\Omega_u^- = \{(2,1), (3,1), (2,2), (3,2), (2,3)\} \quad (29)$$

$$\Omega_v^+ = \{(1,1), (2,1), (3,1), (1,2), (2,2)\} \quad (30)$$

$$\Omega_v^- = \{(1,2), (2,2), (3,2), (1,3), (2,3)\} \quad (31)$$

so that the differentiation matrices $\mathbf{D}_{u/v}^{+/-}$ have five non-zero rows. For instance, the matrix associated with the

forward finite differences operator ∂_u^+ reads:

$$\mathbf{D}_u^+ = \begin{bmatrix} -1 & 1 & 0 & 0 & 0 & 0 & 0 & 0 \\ 0 & -1 & 1 & 0 & 0 & 0 & 0 & 0 \\ 0 & 0 & 0 & 0 & 0 & 0 & 0 & 0 \\ 0 & 0 & 0 & -1 & 1 & 0 & 0 & 0 \\ 0 & 0 & 0 & 0 & -1 & 1 & 0 & 0 \\ 0 & 0 & 0 & 0 & 0 & 0 & 0 & 0 \\ 0 & 0 & 0 & 0 & 0 & 0 & -1 & 1 \\ 0 & 0 & 0 & 0 & 0 & 0 & 0 & 0 \end{bmatrix} \quad (32)$$

The Laplacian matrix \mathbf{L} defined in (21) is worth:

$$\mathbf{L} = \begin{bmatrix} 2 & -1 & 0 & -1 & 0 & 0 & 0 & 0 \\ -1 & 3 & -1 & 0 & -1 & 0 & 0 & 0 \\ 0 & -1 & 2 & 0 & 0 & -1 & 0 & 0 \\ -1 & 0 & 0 & 3 & -1 & 0 & -1 & 0 \\ 0 & -1 & 0 & -1 & 4 & -1 & 0 & -1 \\ 0 & 0 & -1 & 0 & -1 & 2 & 0 & 0 \\ 0 & 0 & 0 & -1 & 0 & 0 & 2 & -1 \\ 0 & 0 & 0 & 0 & -1 & 0 & -1 & 2 \end{bmatrix} \quad (33)$$

One can observe that this matrix describes the connectivity of the graph representing the discrete domain Ω : the diagonal elements $(\mathbf{L})_{i,i}$ are the numbers of neighbors connected to the i -th point, and the off-diagonals elements $(\mathbf{L})_{i,j}$ are worth -1 if the i -th and j -th points are connected, 0 otherwise.

Eventually, the matrices \mathbf{D}_u and \mathbf{D}_v defined in (22) are equal to:

$$\mathbf{D}_u = \frac{1}{2} \begin{bmatrix} -1 & -1 & 0 & 0 & 0 & 0 & 0 & 0 \\ 1 & 0 & -1 & 0 & 0 & 0 & 0 & 0 \\ 0 & 1 & 1 & 0 & 0 & 0 & 0 & 0 \\ 0 & 0 & 0 & -1 & -1 & 0 & 0 & 0 \\ 0 & 0 & 0 & 1 & 0 & -1 & 0 & 0 \\ 0 & 0 & 0 & 0 & 1 & 1 & 0 & 0 \\ 0 & 0 & 0 & 0 & 0 & 0 & -1 & -1 \\ 0 & 0 & 0 & 0 & 0 & 0 & 1 & 1 \end{bmatrix} \quad (34)$$

$$\mathbf{D}_v = \frac{1}{2} \begin{bmatrix} -1 & 0 & 0 & -1 & 0 & 0 & 0 & 0 \\ 0 & -1 & 0 & 0 & -1 & 0 & 0 & 0 \\ 0 & 0 & -1 & 0 & 0 & -1 & 0 & 0 \\ 1 & 0 & 0 & 0 & 0 & 0 & -1 & 0 \\ 0 & 1 & 0 & 0 & 0 & 0 & 0 & -1 \\ 0 & 0 & 1 & 0 & 0 & 1 & 0 & 0 \\ 0 & 0 & 0 & 1 & 0 & 0 & 1 & 0 \\ 0 & 0 & 0 & 0 & 1 & 0 & 1 & 1 \end{bmatrix} \quad (35)$$

Let us now show how these matrices relate to the discretization of the continuous optimality condition (24). Using second-order central finite differences approximations of the Laplacian ($\Delta z_{u,v} \approx z_{u,v-1} + z_{u-1,v} + z_{u+1,v} + z_{u,v+1} - 4z_{u,v}$) and of the divergence operator

$(\nabla \cdot \mathbf{g}_{u,v} \approx \frac{1}{2}(p_{u+1,v} - p_{u-1,v}) + \frac{1}{2}(q_{u,v+1} - q_{u,v-1}))$, we obtain:

$$[4z_{u,v} - z_{u,v-1} - z_{u-1,v} - z_{u+1,v} - z_{u,v+1}] + \lambda_{u,v} z_{u,v} = \frac{1}{2}[p_{u-1,v} - p_{u+1,v}] + \frac{1}{2}[q_{u,v-1} - q_{u,v+1}] + \lambda_{u,v} z_{u,v}^0 \quad (36)$$

The pixel $(u, v) = (2, 2)$ is the only one whose four neighbors are inside Ω . In that case, (36) becomes:

$$\underbrace{[4z_{2,2} - z_{2,1} - z_{1,2} - z_{3,2} - z_{2,3}]}_{=(\mathbf{L})_{5,\mathbf{z}}} + \underbrace{\lambda_{2,2} z_{2,2}}_{=(\mathbf{A}^2)_{5,\mathbf{z}}} = \frac{1}{2} \underbrace{[p_{1,2} - p_{3,2}]}_{=(\mathbf{D}_u)_{5,\mathbf{p}}} + \frac{1}{2} \underbrace{[q_{2,1} - q_{2,3}]}_{=(\mathbf{D}_v)_{5,\mathbf{q}}} + \underbrace{\lambda_{2,2} z_{2,2}^0}_{=(\mathbf{A}^2)_{5,\mathbf{z}^0}} \quad (37)$$

where we recognize the fifth equation of the discrete optimality condition (26). This shows that, for pixels having all four neighbors inside Ω , both the continuous and the discrete variational formulations yield the same discretizations.

Now, let us consider a pixel near the boundary, for instance pixel $(1, 1)$. Using the same second-order differences, (36) reads:

$$[4z_{1,1} - z_{1,0} - z_{0,1} - z_{2,1} - z_{1,2}] + \lambda_{1,1} z_{1,1} = \frac{1}{2}[p_{0,1} - p_{2,1}] + \frac{1}{2}[q_{1,0} - q_{1,2}] + \lambda_{1,1} z_{1,1}^0 \quad (38)$$

which involves the values $z_{1,0}$ and $z_{0,1}$ of the depth map, which we are not willing to estimate, and the values $p_{0,1}$ and $q_{1,0}$ of the gradient field, which are not provided as data. To eliminate these four values, we need to resort to boundary conditions on z , p and q . The discretizations, using first order forward finite differences, of the natural boundary condition (25), at locations $(1, 0)$ and $(0, 1)$, read:

$$z_{1,1} - z_{1,0} = q_{1,0} \quad (39)$$

$$z_{1,1} - z_{0,1} = p_{0,1} \quad (40)$$

hence the unknown depth values $z_{1,0}$ and $z_{0,1}$ can be eliminated from equation (38):

$$[2z_{1,1} - z_{2,1} - z_{1,2}] + \lambda_{1,1} z_{1,1} = \frac{1}{2}[-p_{0,1} - p_{2,1}] + \frac{1}{2}[-q_{1,0} - q_{1,2}] + \lambda_{1,1} z_{1,1}^0 \quad (41)$$

Eventually, the unknown values $p_{0,1}$ and $q_{1,0}$ need to be approximated. Since we have no information at all about the values of \mathbf{g} outside Ω , we use homogeneous Neumann boundary conditions⁶:

$$\nabla p \cdot \boldsymbol{\eta} = 0 \quad \text{over } \partial\Omega \quad (42)$$

$$\nabla q \cdot \boldsymbol{\eta} = 0 \quad \text{over } \partial\Omega \quad (43)$$

⁶ This assumption is weaker than the homogeneous Neumann boundary condition $\nabla z \cdot \boldsymbol{\eta} = 0$ used, e.g., in [1].

Discretizing these boundary conditions using first order forward finite differences, we obtain:

$$p_{0,1} = p_{1,1} \quad (44)$$

$$q_{1,0} = q_{1,1} \quad (45)$$

The discretized optimality condition (41) becomes:

$$\underbrace{[2z_{1,1} - z_{2,1} - z_{1,2}]}_{=(\mathbf{L})_{1,\mathbf{z}}} + \underbrace{\lambda_{1,1} z_{1,1}}_{=(\mathbf{A}^2)_{1,\mathbf{z}}} = \frac{1}{2} \underbrace{[-p_{1,1} - p_{2,1}]}_{=(\mathbf{D}_u)_{1,\mathbf{p}}} + \frac{1}{2} \underbrace{[-q_{1,1} - q_{1,2}]}_{=(\mathbf{D}_v)_{1,\mathbf{q}}} + \underbrace{\lambda_{1,1} z_{1,1}^0}_{=(\mathbf{A}^2)_{1,\mathbf{z}^0}} \quad (46)$$

which is exactly the first equation of the discrete optimality condition (26).

Using a similar rationale, we obtain equivalence of both formulations for the eight points inside Ω . Yet, let us emphasize that discretizing the continuous optimality condition requires treating, on this example with a rather “simple” shape for Ω , not less than seven different cases (only $(3, 2)$ and $(2, 3)$ are similar). More general shapes bring out to play even more particular cases (points having only one neighbor inside Ω). Furthermore, boundary conditions must be invoked in order to approximate the depth values and the data outside Ω . On the other hand, the discrete functional provides exactly the same optimality condition, but without these drawbacks. The boundary conditions can be viewed as *implicitly* enforced, hence $\mathcal{P}_{\text{FreeB}}$ is satisfied.

2.5 Empirical Evaluation

We first consider the smooth surface from figure 2, whose normals are analytically known, and compare three discrete least-squares methods which all satisfy $\mathcal{P}_{\text{Fast}}$, $\mathcal{P}_{\text{Robust}}$ and $\mathcal{P}_{\text{FreeB}}$: the DCT solution [53], the Sylvester equations method [27], and the proposed one. Since all these methods are based on least-squares, they all provide robustness to additive Gaussian noise. Yet, as shown in figure 3, our solution is slightly more accurate, thanks to the new discretization. Indeed, the bias near the boundary induced by the DCT method is corrected. On the other hand, we believe the reason why our method is more accurate than that from [27] is because we use first-order finite differences approximation of the gradient, while [27] relies on central differences: the second-order operators (Laplacian and divergence) implicitly involved in the Sylvester equations from [27] are not rotationally invariant. Although using second-order finite differences induces an improved accuracy with $\sigma = 0$, the lack of rotational invariance may become problematic in the presence of noise.

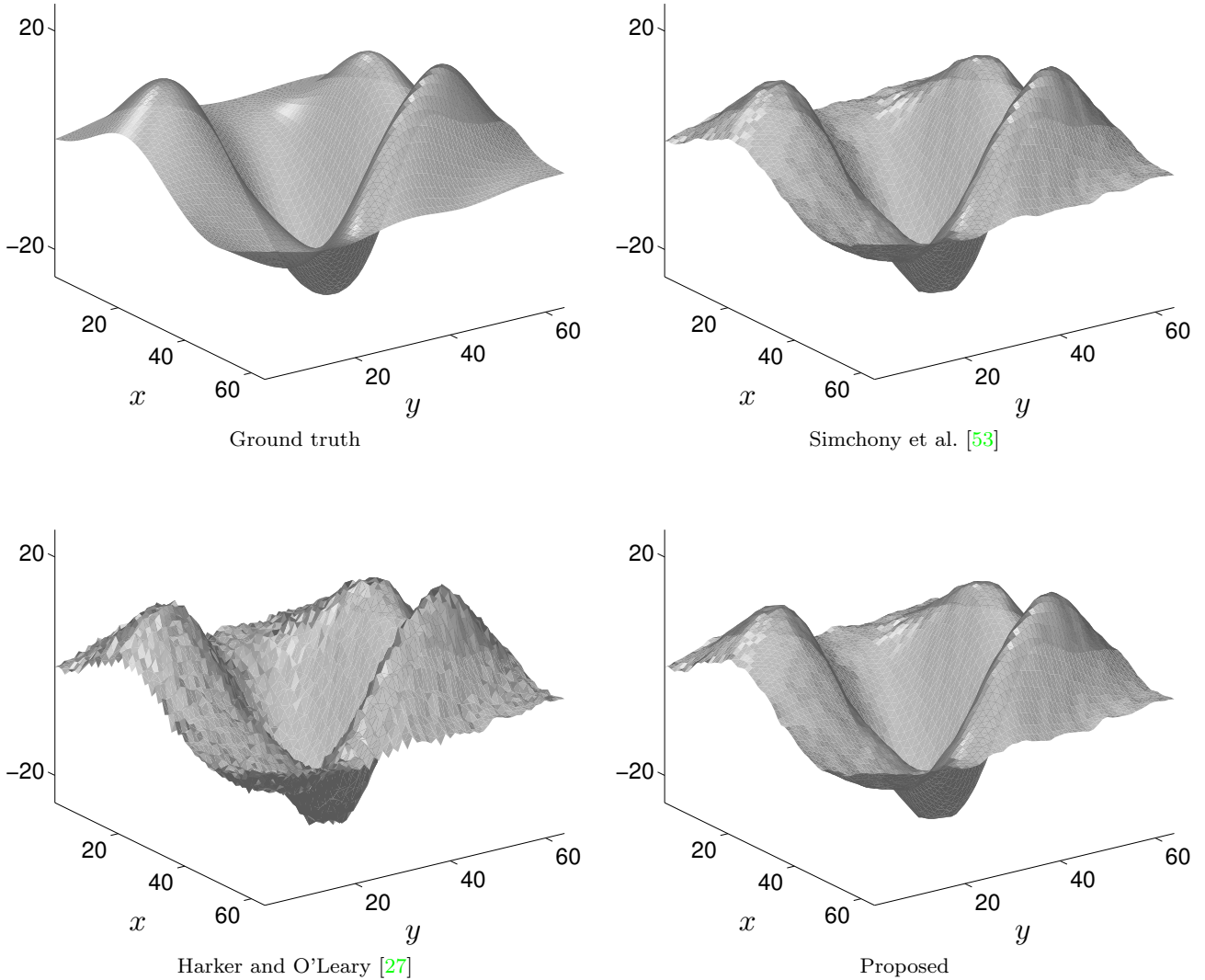


Fig. 2 Qualitative evaluation of the $\mathcal{P}_{\text{Robust}}$ property. An additive, zero-mean, Gaussian noise with standard deviation $0.1\|\mathbf{g}\|_{\infty}$ was added to the (analytically known) gradient of the ground truth surface, before integrating this gradient by three least-squares methods. Ours qualitatively provides better results than the Sylvester equations method from Harker and O’Leary [27]. It seems to provide similar robustness as the DCT solution from Simchony et al. [53], but the quantitative evaluation from figure 3 shows that our method is actually more accurate.

In addition, as predicted by the complexity analysis in subsection 2.2, our solution relying on preconditioned conjugate gradient iterations has a slightly lower asymptotic complexity ($O(5|\Omega| \log |\Omega| \log(1/\epsilon))$) than [27] ($O(|\Omega|^{1.5})$) and [53] ($O(|\Omega| \log |\Omega|)$). The CPU times of our method and of the DCT solution, measured using Matlab codes running on a recent i7 processor, actually seem proportional: according to our complexity analysis, we guess the proportionality constant is around $5 \log(1/\epsilon)$. Indeed, with $\epsilon = 10^{-4}$, which is the value we used in our experiments, $5 \log(1/\epsilon) \approx 46$, which is consistent with the second graph in figure 3.

Besides its improved accuracy, the major advantage of our method over [27, 53] is its ability to handle non-rectangular domains ($\mathcal{P}_{\text{NoRect}}$). As discussed in our survey paper [19], this makes possible the 3D-reconstruction of piecewise-smooth surfaces, provided that a user segments the domain into pieces where z is smooth beforehand (cf. figure 4). Yet, if the segmentation is not a priori performed, artifacts are visible near the discontinuities, which get smoothed, and Gibbs phenomena appear near the continuous, yet non-differentiable kinks. We will discuss in the next section several strategies for removing such artifacts.

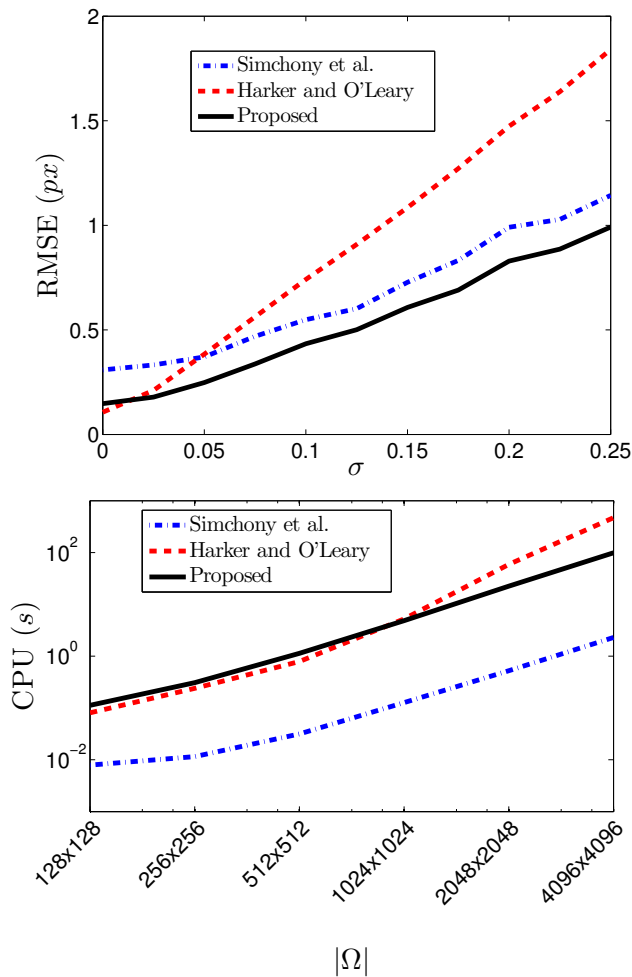


Fig. 3 Quantitative evaluation of the $\mathcal{P}_{\text{Robust}}$ (top) and $\mathcal{P}_{\text{Fast}}$ (bottom) properties. Top: RMSE between the ground truth depth map and the ones reconstructed from noisy gradients (adding a zero-mean Gaussian noise with standard deviation $\sigma \|\mathbf{g}\|_{\infty}$). Our discretization provides more accurate results than existing least-squares methods. Bottom: the complexity of our approach is inbetween those of the methods of Simchony et al. [53] (based on DCT) and of Harker and O’Leary [27] (based on Sylvester equations).

Overall, we have introduced a quadratic integration method, which is robust to Gaussian noise ($\mathcal{P}_{\text{Robust}}$), with a discretization enforcing both $\mathcal{P}_{\text{FreeB}}$ and $\mathcal{P}_{\text{NoRect}}$. We have shown how to solve the associated optimality condition for a complexity which is slightly higher than $O(|\Omega| \log |\Omega|)$, using the preconditioned conjugate gradient technique ($\mathcal{P}_{\text{Fast}}$). Eventually, its basic version where no a priori is introduced is parameter-free ($\mathcal{P}_{\text{NoPar}}$), but it also allows taking into account prior knowledge of the solution, by appropriately tuning the parameters (cf. subsection 1.5). All properties except $\mathcal{P}_{\text{Disc}}$ are thus satisfied. In the next section, we discuss several strategies for satisfying this property.

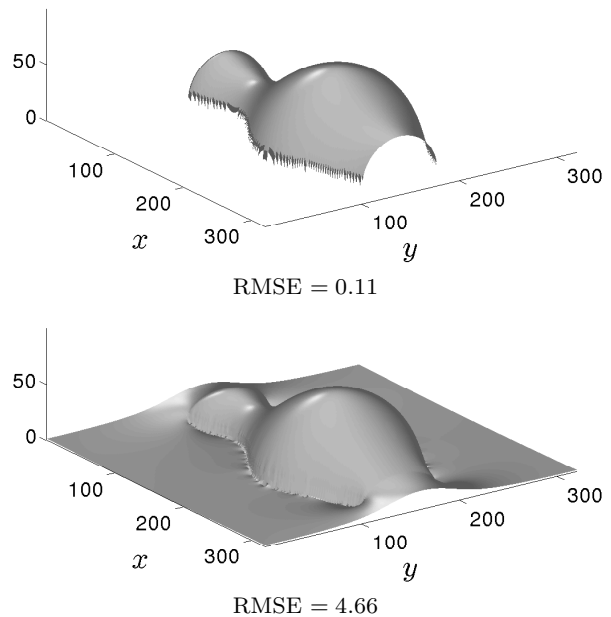


Fig. 4 3D-reconstruction of surface $\mathcal{S}_{\text{vase}}$ from its (analytically known) normals (see figure 3 in [19]), using the proposed discrete least-squares method. Top: when Ω is restricted to the vase. Bottom: when Ω is the whole rectangular grid. Quadratic integration smooths the depth discontinuities and produces Gibbs phenomena near the kinks.

3 Piecewise Smooth Surfaces

We now tackle the problem of recovering a surface which is smooth only *almost* everywhere, i.e. everywhere except on a “small” set where discontinuities and kinks are allowed. Since all the methods discussed hereafter rely on the same discretization as in section 2, they inherit its $\mathcal{P}_{\text{FreeB}}$ and $\mathcal{P}_{\text{NoRect}}$ properties, which will not be discussed in this section. Instead, we focus on the $\mathcal{P}_{\text{Fast}}$, $\mathcal{P}_{\text{Robust}}$, $\mathcal{P}_{\text{NoPar}}$, and of course $\mathcal{P}_{\text{Disc}}$ properties.

3.1 Proposed Strategies for Recovering Discontinuities and Kinks

In order to clarify which variational formulations may provide robustness to discontinuities, let us first consider the 1D-example of figure 5, with Dirichlet boundary conditions. As illustrated in this example, least-squares integration of a noisy normal field will provide a smooth surface. On the other hand, replacing the least-squares estimator $\Phi_{L_2}(s) = s^2$ by the sparsity estimator $\Phi_{L_0}(s) = 1 - \delta(s)$ will minimize the cardinality of the difference between \mathbf{g} and ∇z , which provides a surface whose gradient is almost everywhere equal to \mathbf{g} . As a consequence, robustness to noise is lost, yet discontinuities may be preserved.

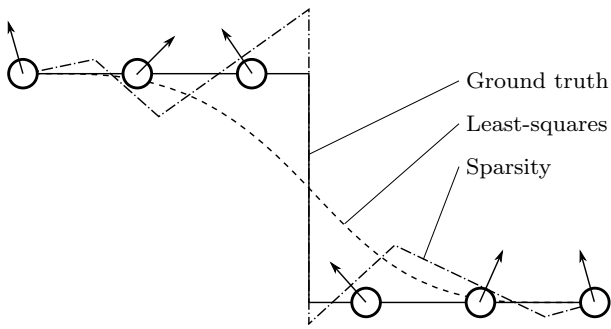


Fig. 5 1D-illustration of integration of a noisy normal field (arrows) over a regular grid (circles), in the presence of discontinuities. The least-squares approach is robust to noise, but smooths the discontinuities. The sparsity approach preserves the discontinuities, but is not robust to noise. An ideal integration method would inherit robustness from least-squares, and the ability to preserve discontinuities from sparsity.

These estimators can be interpreted in the following way: least-squares assume that *all* residuals defined by $\|\nabla z(u, v) - \mathbf{g}(u, v)\|$ are “low”, while sparsity assumes that *most of* them are “zero”. The former assumption is commonly used for “noise”, and the latter for “outliers”. In the case of normal integration, such outliers can occur when: 1) $\nabla z(u, v)$ exists but its estimate $\mathbf{g}(u, v)$ is not reliable; 2) $\nabla z(u, v)$ is not defined because (u, v) lies within the vicinity of a discontinuity or a kink. Considering that situation 1) should rather be handled by robust estimation of the gradient [32], we deal only with the second one. From now on, we use the terminology “discontinuity” instead of “outlier”, although this also covers the concept of “kink”.

We are looking for an estimator which combines the robustness of least-squares to noise, and that of sparsity to discontinuities. These abilities are actually due to their asymptotic behaviors. Robustness of least-squares to noise comes from the quadratic behavior around 0, which ensures that “low” residuals are considered as “good” estimates, while this quadratic behavior becomes problematic in $\pm\infty$: discontinuities yield “high” residuals, which are over-penalized. The sparsity estimator has the opposite behavior: treating the high residuals (discontinuities) exactly as the low ones ensures that discontinuities are not over-penalized, yet low residuals (noise) are. A good estimator would thus be quadratic around zero, but sub-linear around $\pm\infty$. Obviously, only non-convex estimators hold both these properties. We will discuss several choices “inbetween” the quadratic estimator Φ_{L_2} and the sparsity one Φ_{L_0} (cf. figure 6): the convex compromise $\Phi_{L_1}(s) = |s|$ is studied in subsection 3.2, and the non-convex estimators $\Phi_1(s) = \log(s^2 + \beta^2)$ and $\Phi_2(s) = \frac{s^2}{s^2 + \gamma^2}$, where β and γ are hyper-parameters, in subsection 3.3.

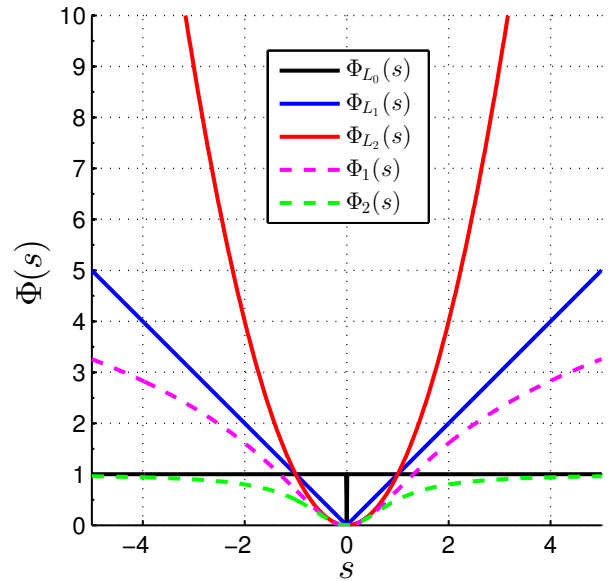


Fig. 6 Graph of some robust estimators. The ability of Φ_{L_2} to handle noise (small residuals) comes from its over-linear behavior around zero, while that of Φ_{L_0} to preserve discontinuities (large residuals) is induced by its sub-linear behavior in $+\infty$. An estimator holding both these properties is necessarily non-convex (e.g., Φ_1 and Φ_2 , whose graphs are shown with $\beta = \gamma = 1$), although Φ_{L_1} may be an acceptable convex compromise.

Another strategy consists in keeping least-squares as basis for the integration, but using it in a non-uniform manner. The simplest way would be to remove the discontinuity points from the integration domain Ω , and then to apply our quadratic method from the previous section, since it is able to manage non-rectangular domains. Yet, this would require a priori detection of discontinuities, which might be tedious. It is actually more convenient to introduce weights in the least-squares functionals, with weights inversely proportional to the probability of lying on a discontinuity [48, 50]. We discuss this weighted least-squares approach in subsection 3.4, where a statistical interpretation of the Perona and Malik’s anisotropic diffusion model [45] is also exhibited. Eventually, an extreme case of weighted least-squares consists in using binary weights, where the weights indicate the presence of discontinuities. This is closely related to Mumford and Shah’s segmentation method [38], which simultaneously estimates the discontinuity set and the surface. We show in subsection 3.5 that this approach is the one which is actually the most adapted to the problem of integrating a noisy normal field in the presence of discontinuities.

3.2 Total Variation-like Integration

The problem of handling outliers in a noisy normal field has been tackled by Du, Robles-Kelly and Lu, who compare in [17] the performances of several M-estimators. They conclude that regularizers based on the L_1 norm are the most effective ones. We provide in this subsection several numerical considerations regarding the discretization of the L_1 fidelity term:

$$\begin{aligned} \mathcal{F}_{L_1}(z) &= \iint_{(u,v) \in \Omega} \|\nabla z(u,v) - \mathbf{g}(u,v)\|_1 du dv \\ &= \iint_{(u,v) \in \Omega} \left\{ |\partial_u z(u,v) - p(u,v)| \right. \\ &\quad \left. + |\partial_v z(u,v) - q(u,v)| \right\} du dv \end{aligned} \quad (47)$$

When $p(u,v) \equiv 0$ and $q(u,v) \equiv 0$, (47) is the so-called ‘‘anisotropic total variation’’ (anisotropic TV) regularizer, which tends to favor piecewise-constant solutions while allowing discontinuity jumps. Considering the discontinuities and kinks as the equivalent of edges in image restoration, it seems natural to believe that the fidelity term (47) may be useful for discontinuity-preserving integration.

This fidelity term is not only convex, but also decouples the two directions u and v , which allows fast ADMM-based (Bregman iterations) numerical schemes involving shrinkages [25, 48]. On the other hand, it is not so natural to use such a decoupling: if the value of p is not reliable at some point (u,v) , usually that of q is not reliable either. Hence, it may be worthwhile to use instead a regularizer adapted from the ‘‘isotropic TV’’. This leads us to adapt the infamous model from Rudin, Osher and Fatemi [49] to the integration problem:

$$\begin{aligned} \mathcal{E}_{\text{TV}}(z) &= \iint_{(u,v) \in \Omega} \|\nabla z(u,v) - \mathbf{g}(u,v)\| \\ &\quad + \lambda(u,v) [z(u,v) - z^0(u,v)]^2 du dv \end{aligned} \quad (48)$$

Discretization. Since the term $\|\nabla z(u,v) - \mathbf{g}(u,v)\|$ can be interpreted in different manners, depending on the neighborhood of (u,v) , we need to discretize it appropriately. Let us consider all four possible first-order discretizations of the gradient ∇z , associated to the four following sets of pixels:

$$\Omega^{UV} = \Omega_u^U \cap \Omega_v^V, \quad (U, V) \in \{+, -\}^2 \quad (49)$$

The discrete functional to minimize is thus given by:

$$\begin{aligned} E_{\text{TV}}(\mathbf{z}) &= \frac{1}{4} \left(\sum_{(u,v) \in \Omega^{++}} \sqrt{[\partial_u^+ z_{u,v} - p_{u,v}]^2 + [\partial_v^+ z_{u,v} - q_{u,v}]^2} \right. \\ &\quad + \sum_{(u,v) \in \Omega^{+-}} \sqrt{[\partial_u^+ z_{u,v} - p_{u,v}]^2 + [\partial_v^- z_{u,v} - q_{u,v}]^2} \\ &\quad + \sum_{(u,v) \in \Omega^{-+}} \sqrt{[\partial_u^- z_{u,v} - p_{u,v}]^2 + [\partial_v^+ z_{u,v} - q_{u,v}]^2} \\ &\quad \left. + \sum_{(u,v) \in \Omega^{--}} \sqrt{[\partial_u^- z_{u,v} - p_{u,v}]^2 + [\partial_v^- z_{u,v} - q_{u,v}]^2} \right) \\ &\quad + \sum_{(u,v) \in \Omega} \lambda_{u,v} [z_{u,v} - z_{u,v}^0]^2 \end{aligned} \quad (50)$$

Minimizing (50) comes down to solving the following constrained optimization problem:

$$\begin{aligned} \min_{\mathbf{z}, \{\mathbf{r}^{UV}\}} & \frac{1}{4} \sum_{(U,V) \in \{+,-\}^2} \sum_{(u,v) \in \Omega^{UV}} \|\mathbf{r}_{u,v}^{UV}\| \\ & + \sum_{(u,v) \in \Omega} \lambda_{u,v} [z_{u,v} - z_{u,v}^0]^2 \\ \text{s.t.} & \quad \mathbf{r}_{u,v}^{UV} = \nabla^{UV} z_{u,v} - \mathbf{g}_{u,v} \end{aligned} \quad (51)$$

where we denote $\nabla^{UV} = [\partial_u^U, \partial_v^V]^\top$, $(U, V) \in \{+, -\}^2$, the discrete approximation of the gradient corresponding to domain Ω^{UV} .

Numerical Resolution. We solve the constrained optimization problem (51) by the augmented Lagrangian method, through an ADMM algorithm [22] (see [7] for a recent overview of such algorithms). This algorithm reads:

$$\begin{aligned} \mathbf{z}^{(k+1)} &= \underset{\mathbf{z} \in \mathbb{R}^{|\Omega|}}{\text{argmin}} \frac{\alpha}{8} \sum_{(U,V) \in \{+,-\}^2} \sum_{(u,v) \in \Omega^{UV}} \left\| \nabla^{UV} z_{u,v} \right. \\ &\quad \left. - \left(\mathbf{g}_{u,v} + \mathbf{r}_{u,v}^{UV(k)} - \mathbf{b}_{u,v}^{UV(k)} \right) \right\|^2 \\ &\quad + \sum_{(u,v) \in \Omega} \lambda_{u,v} [z_{u,v} - z_{u,v}^0]^2 \end{aligned} \quad (52)$$

$$\begin{aligned} \mathbf{r}_{u,v}^{UV(k+1)} &= \underset{\mathbf{r} \in \mathbb{R}^2}{\text{argmin}} \frac{\alpha}{8} \left\| \mathbf{r} - \left(\nabla^{UV} z_{u,v}^{(k+1)} - \mathbf{g}_{u,v} + \mathbf{b}_{u,v}^{UV(k)} \right) \right\|^2 \\ &\quad + \|\mathbf{r}\| \end{aligned} \quad (53)$$

$$\mathbf{b}_{u,v}^{UV(k+1)} = \mathbf{b}_{u,v}^{UV(k)} + \nabla^{UV} z_{u,v}^{(k+1)} - \mathbf{g}_{u,v} - \mathbf{r}_{u,v}^{UV(k+1)} \quad (54)$$

where the \mathbf{b}^{UV} are the scaled dual variables, and $\alpha > 0$ corresponds to a descent stepsize, which is supposed to be fixed beforehand. Note that the choice of this parameter influences only the convergence rate, not the actual minimizer. In our experiments, we used $\alpha = 1$.

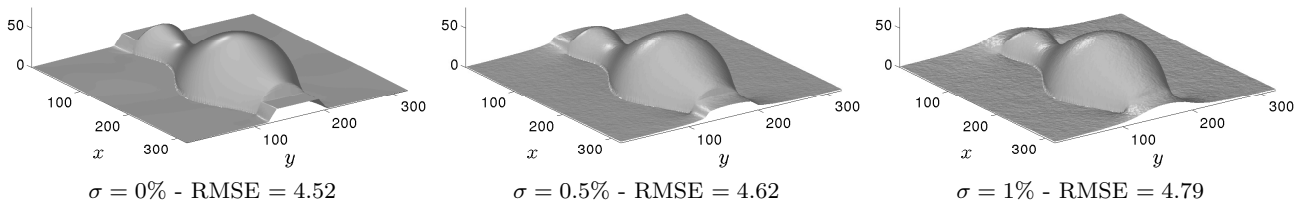


Fig. 7 Depth estimated after $k = 1000$ iterations of the TV-like approach, in the presence of additive, zero-mean, Gaussian noise with standard deviation equal to $\sigma \|\mathbf{g}\|_\infty$. The indicated RMSE is computed on the whole domain. In the absence of noise, both discontinuities and kinks are restored, although staircasing artifacts appear. In the presence of noise, the discontinuities are smoothed. Yet, the 3D-reconstruction near the kinks is still more satisfactory than the least-squares one: Gibbs phenomena are not visible, unlike in the second row of Fig. 4.

The z -update (52) is a linear least-squares problem similar to the one which was tackled in section 2. Its solution $\mathbf{z}^{(k+1)}$ is the solution of the following SDD linear system:

$$\mathbf{A}_{\text{TV}} \mathbf{z}^{(k+1)} = \mathbf{b}_{\text{TV}}^{(k)} \quad (55)$$

with :

$$\mathbf{A}_{\text{TV}} = \frac{\alpha}{8} \sum_{(U,V) \in \{+,-\}^2} \left[\mathbf{D}_u^{U\top} \mathbf{D}_u^U + \mathbf{D}_v^{V\top} \mathbf{D}_v^V \right] + \mathbf{A}^2 \quad (56)$$

$$\mathbf{b}_{\text{TV}}^{(k)} = \frac{\alpha}{8} \sum_{(U,V) \in \{+,-\}^2} \left[\mathbf{D}_u^{U\top} \mathbf{p}^{UV(k)} + \mathbf{D}_v^{V\top} \mathbf{q}^{UV(k)} \right] + \mathbf{A}^2 \mathbf{z}^0 \quad (57)$$

where the $\mathbf{D}_{u/v}^{U/V}$ matrices are defined as in (15), the \mathbf{A} matrix as in (18), and where we denote $\mathbf{p}^{UV(k)}$ and $\mathbf{q}^{UV(k)}$ the components of $\mathbf{g} + \mathbf{r}^{UV(k)} - \mathbf{b}^{UV(k)}$.

The solution of system (55) can be approximated by a few conjugate gradient iterations. At each iteration, the previous estimate $\mathbf{z}^{(k)}$ can be chosen as initial guess (setting $\mathbf{z}^{(0)}$, for instance, as the least-squares solution from section 2). It should also be emphasized that, although the second member $\mathbf{b}_{\text{TV}}^{(k)}$ has to be updated at each iteration, the matrix \mathbf{A}_{TV} is always the same: this allows computing the preconditioner only once.

Eventually, the \mathbf{r} -updates (53), $(u, v) \in \Omega$, are basis pursuit problems [16], which admit the following closed-form solution (generalized shrinkage):

$$\mathbf{r}_{u,v}^{UV(k+1)} = \max \left\{ \left\| \mathbf{s}_{u,v}^{UV(k+1)} \right\| - \frac{4}{\alpha}, 0 \right\} \frac{\mathbf{s}_{u,v}^{UV(k+1)}}{\left\| \mathbf{s}_{u,v}^{UV(k+1)} \right\|} \quad (58)$$

with:

$$\mathbf{s}_{u,v}^{UV(k+1)} = \nabla^{UV} z_{u,v}^{(k+1)} - \mathbf{g}_{u,v} + \mathbf{b}_{u,v}^{UV(k)} \quad (59)$$

Discussion. This TV-like approach has two main advantages: apart from the stepsize α which controls the speed of convergence, it does not depend on the choice of a parameter, and it is convex. The initialization has influence only on the speed of convergence, and not on the actual minimizer: the ADMM scheme we use guarantees convergence towards the global minimum [51]. Eventually, it can be shown that the convergence rate of this scheme is ergodic, and this rate can be improved by rather simple modifications [24]. We cannot consider that $\mathcal{P}_{\text{Fast}}$ is satisfied since, in comparison with the quadratic method from section 2, yet the TV approach is “reasonably” fast. For completeness, let us state that other optimization strategies can be considered for the TV approach: the FISTA algorithm from Beck and Teboulle [5], and primal-dual algorithms such as that proposed by Chambolle and Pock [12]. These algorithms may be faster regarding our problem, but we leave such a comparison as future work.

On the other hand, according to the results from figure 7, discontinuities are recovered in the absence of noise, although staircasing artifacts appear (such artifacts are partly due to the non-differentiability of TV in zero [39]). Yet, the recovery of discontinuities is deceiving when the noise level increases. On noisy datasets, the only advantage of this approach over least-squares is thus that it removes the Gibbs phenomena around the kinks i.e., where the surface is continuous, but non-differentiable (e.g., the sides of the vase).

Because of the staircasing artifacts and of the lack of robustness to noise, we cannot find this first approach satisfactory. Yet, since turning the quadratic functional into a non-quadratic one seems to have positive influence on discontinuities recovery, we believe that exploring non-quadratic models is a promising route. In order to remove the staircasing artifacts, total variation could be replaced by total generalized variation (TGV) [8]. We choose to consider other non-quadratic models, namely non-convex ones.

3.3 Non-convex Regularization

Let us now consider non-convex estimators Φ in the fidelity term (5), which are often referred to as “ Φ -functions” [3]. As discussed in subsection 3.1, the choice of a specific Φ -function should be made according to several principles:

- Φ should have a quadratic behavior around zero, in order to ensure that the integration is guided by the “good” data. The typical choice ensuring this property is $\Phi_{L_2}(s) = s^2$, which was discussed in section 2;
- Φ should have a sublinear behavior at infinity, so that outliers do not have a predominant influence, and also to preserve discontinuities and kinks. The typical choice is the sparsity estimator $\Phi_{L_0}(s) = 0$ if $s = 0$ and $\Phi_{L_0}(s) = 1$ otherwise;
- Φ should ideally be a convex function.

Obviously, it is not possible to simultaneously satisfy these three properties. The TV-like fidelity term introduced in subsection 3.2 is a sort of “compromise”: it is the only convex function being (over-) linear in 0 and (sub-) linear in $\pm\infty$. Although it does not depend on the choice of any hyper-parameter, we saw that it has the drawback of yielding the so-called “staircase effect”, and that discontinuities were not recovered so well in the presence of noise. If we accept to lose the convex property of Φ , we can actually design estimators which better fit both other properties. Although there may then be several minimizers, such non-convex estimators were recently shown to be very effective for image restoration [37].

We will consider two classical Φ -functions, whose graphs are plotted in figure 6:

$$\begin{cases} \Phi_1(s) = \log(s^2 + \beta^2) \\ \Phi_2(s) = \frac{s^2}{s^2 + \gamma^2} \end{cases} \Rightarrow \begin{cases} \Phi'_1(s) = \frac{2s}{s^2 + \beta^2} \\ \Phi'_2(s) = \frac{2\gamma^2 s}{(s^2 + \gamma^2)^2} \end{cases} \quad (60)$$

Let us remark that these estimators were initially introduced in [18] in this context, and that other non-convex estimators can be considered, based for instance on L^p norms, with $0 < p < 1$ [4].

Let us now show how to numerically minimize the resulting functionals:

$$\begin{aligned} \mathcal{E}_\Phi(z) = & \iint_{(u,v) \in \Omega} \Phi(\|\nabla z(u,v) - \mathbf{g}(u,v)\|) \\ & + \lambda(u,v) [z(u,v) - z^0(u,v)]^2 \, du \, dv \quad (61) \end{aligned}$$

Discretization. We consider the same discretization strategy as in subsection 3.2, aiming at minimizing the discrete functional:

$$\begin{aligned} E_\Phi(\mathbf{z}) = & \frac{1}{4} \sum_{(U,V) \in \{+,-\}^2} \sum_{(u,v) \in \Omega^{UV}} \Phi(\|\nabla^{UV} z_{u,v} - \mathbf{g}_{u,v}\|) \\ & + \sum_{(u,v) \in \Omega} \lambda_{u,v} [z_{u,v} - z_{u,v}^0]^2 \quad (62) \end{aligned}$$

which resembles the TV functional defined in (50), and where ∇^{UV} represents the finite differences approximation of the gradient used over the domain Ω^{UV} , with $\{U, V\} \in \{+, -\}^2$.

Introducing the notations:

$$f(\mathbf{z}) = \frac{1}{4} \sum_{(U,V) \in \{+,-\}^2} \sum_{(u,v) \in \Omega^{UV}} \Phi(\|\nabla^{UV} z_{u,v} - \mathbf{g}_{u,v}\|) \quad (63)$$

$$g(\mathbf{z}) = \|\mathbf{A}(\mathbf{z} - \mathbf{z}^0)\|^2 \quad (64)$$

the discrete functional (62) is rewritten:

$$E_\Phi(\mathbf{z}) = f(\mathbf{z}) + g(\mathbf{z}) \quad (65)$$

where f is smooth, but *non-convex*, and g is *convex* (and smooth, although non-smooth functions g could be handled using the “iPiano” framework detailed hereafter).

Numerical resolution. The problem of minimizing a discrete energy like (65), yielded by the sum of a convex term g and a non-convex, yet smooth term f , can be handled by forward-backward splitting. We use the “iPiano” iterative algorithm by Ochs et al. [42], which reads:

$$\mathbf{z}^{(k+1)} = (\mathbf{I} + \alpha_1 \partial g)^{-1} \left(\mathbf{z}^{(k)} - \alpha_1 \nabla f(\mathbf{z}^{(k)}) + \alpha_2 (\mathbf{z}^{(k)} - \mathbf{z}^{(k-1)}) \right) \quad (66)$$

where α_1 and α_2 are suitable descent stepsizes (in our implementation, α_2 is fixed to 0.8, and α_1 is chosen by the “lazy backtracking” procedure described in [42]), $(\mathbf{I} + \alpha_1 \partial g)^{-1}$ is the *proximal operator* of g , and $\nabla f(\mathbf{z}^{(k)})$ is the gradient of f evaluated at current estimate $\mathbf{z}^{(k)}$. We detail hereafter how to evaluate the proximal operator of g and the gradient of f .

The proximal operator of g writes, using (64):

$$(\mathbf{I} + \alpha_1 \partial g)^{-1}(\hat{\mathbf{x}}) = \operatorname{argmin}_{\mathbf{x} \in \mathbb{R}^{|\Omega^1|}} \frac{\|\mathbf{x} - \hat{\mathbf{x}}\|}{2} + \alpha_1 g(\mathbf{x}) \quad (67)$$

$$= (\mathbf{I} + 2\alpha_1 \mathbf{A}^2)^{-1} (\hat{\mathbf{x}} + 2\alpha_1 \mathbf{A} \mathbf{z}^0) \quad (68)$$

where the inversion is easy to compute, since the matrix involved is diagonal.

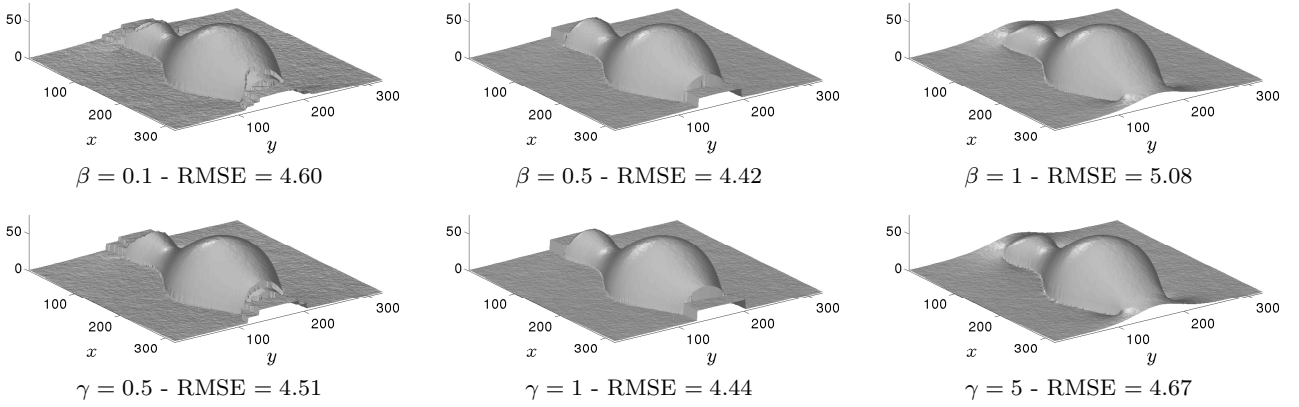


Fig. 8 Non-convex 3D-reconstruction of surface $\mathcal{S}_{\text{vase}}$, using Φ_1 (top) or Φ_2 (bottom). An additive, zero-mean, Gaussian noise with standard deviation $\sigma \|\mathbf{g}\|_\infty$, $\sigma = 1\%$, was added to the gradient field. The non-convex approaches depend on the tuning of a parameter (β or γ), but they are able to reconstruct the discontinuities in the presence of noise, contrarily to the TV-like approach. Staircasing artifacts indicate the presence of local minima (we used as initial guess $z^{(0)}$ the least-squares solution).

In order to obtain a closed-form expression of the gradient of f defined in (63), let us rewrite this function in the following manner:

$$f(\mathbf{z}) = \frac{1}{4} \sum_{(U,V) \in \{+,-\}^2} \sum_{(u,v) \in \Omega^{UV}} \Phi(\|\mathbf{D}_{u,v}^{UV} \mathbf{z} - \mathbf{g}_{u,v}\|) \quad (69)$$

where $\mathbf{D}_{u,v}^{UV}$ is a $2 \times |\Omega|$ finite differences matrix used for approximating the gradient at location (u, v) , using the finite differences operator ∇^{UV} , $\{U, V\} \in \{+, -\}^2$:

$$\mathbf{D}_{u,v}^{UV} = \begin{bmatrix} (\mathbf{D}_u^U)_{m^{-1}(u,v), \cdot} \\ (\mathbf{D}_v^V)_{m^{-1}(u,v), \cdot} \end{bmatrix} \quad (70)$$

where we recall that the mapping m associates linear indices with pixel coordinates (cf. equation (16)).

The gradient of f is thus given by:

$$\nabla f(\mathbf{z}) = \frac{1}{4} \sum_{(U,V) \in \{+,-\}^2} \sum_{(u,v) \in \Omega^{UV}} \left\{ \mathbf{D}_{u,v}^{UV \top} (\mathbf{D}_{u,v}^{UV} \mathbf{z} - \mathbf{g}_{u,v}) \times \frac{\Phi'(\|\mathbf{D}_{u,v}^{UV} \mathbf{z} - \mathbf{g}_{u,v}\|)}{\|\mathbf{D}_{u,v}^{UV} \mathbf{z} - \mathbf{g}_{u,v}\|} \right\} \quad (71)$$

Given the choices (60) for the Φ -functions, this can be further simplified:

$$\nabla f_1(\mathbf{z}) = \frac{1}{2} \sum_{(U,V) \in \{+,-\}^2} \sum_{(u,v) \in \Omega^{UV}} \frac{\mathbf{D}_{u,v}^{UV \top} (\mathbf{D}_{u,v}^{UV} \mathbf{z} - \mathbf{g}_{u,v})}{\|\mathbf{D}_{u,v}^{UV} \mathbf{z} - \mathbf{g}_{u,v}\|^2 + \beta^2} \quad (72)$$

$$\nabla f_2(\mathbf{z}) = \frac{1}{2} \sum_{(U,V) \in \{+,-\}^2} \sum_{(u,v) \in \Omega^{UV}} \frac{\gamma^2 \mathbf{D}_{u,v}^{UV \top} (\mathbf{D}_{u,v}^{UV} \mathbf{z} - \mathbf{g}_{u,v})}{(\|\mathbf{D}_{u,v}^{UV} \mathbf{z} - \mathbf{g}_{u,v}\|^2 + \gamma^2)^2} \quad (73)$$

Discussion. Contrarily to the TV-like approach (subsection 3.2), the non-convex estimators require setting one hyper-parameter (β or γ). As shown in figure 8, the choice of this parameter is crucial: when it is too high, discontinuities are smoothed, while setting a too low value leads to strong staircasing artifacts. Inbetween, the values $\beta = 0.5$ and $\gamma = 1$ seem to preserve discontinuities, even in the presence of noise (which was not the case using the TV-like approach).

Yet, staircasing artifacts are still present. Despite their non-convexity, the new estimators Φ_1 and Φ_2 are differentiable, hence these artifacts do not come from a lack of differentiability, as this was the case for TV. They rather indicate the presence of local minima. This is illustrated in figure 9, where the 3D-reconstruction of a “Canadian tent”-like surface, with additive, zero-mean, Gaussian noise ($\sigma = 10\%$), is presented. When using the least-squares solution as initial guess $z^{(0)}$, the 3D-reconstruction is very close to the genuine surface. Yet, when using the trivial initialization $z^{(0)} \equiv 0$, we obtain a surface whose slopes are “almost everywhere” equal to the real ones, but unexpected discontinuity jumps appear. Since only the initialization differs in these experiments, this clearly shows that the artifacts indicate the presence of local minima.

Although local minima can sometimes be avoided by using the least-squares solution as initial guess (e.g., figure 9), this is not always the case (e.g., figure 8). Hence, the non-convex estimators perform overall better than the TV-like approach, but they are still not optimal. We now follow other routes, which use least-squares as basis estimator, yet in a non-uniform manner, in order to allow discontinuities.

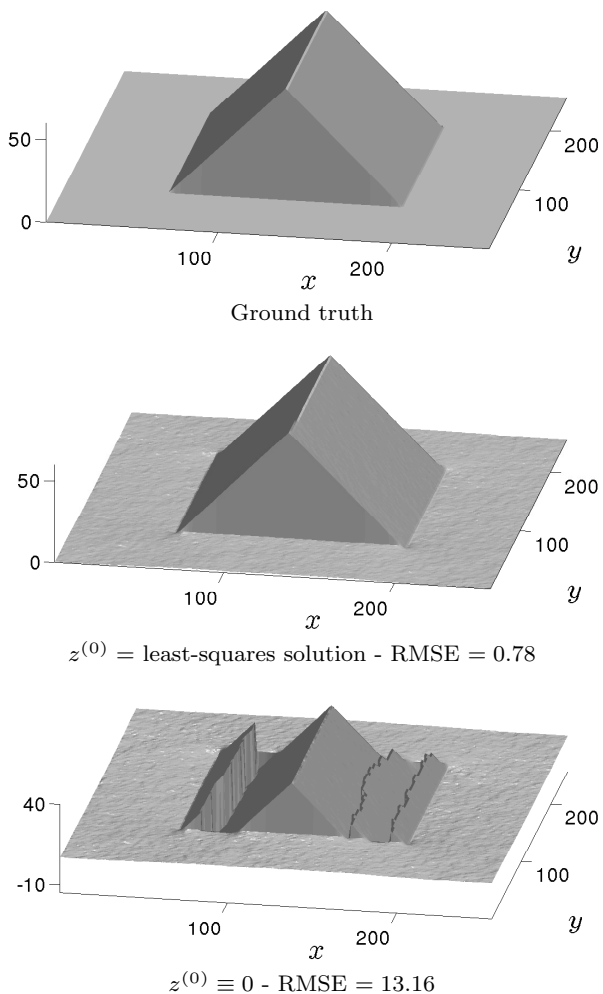


Fig. 9 3D-reconstruction of a “Canadian tent”-like surface by the non-convex integrator Φ_1 ($\beta = 0.5$, $k = 12000$ iterations), using two different initializations. The objective function being non-convex, the iterative scheme may converge towards a local minimum.

3.4 Integration by Anisotropic Diffusion

Both previous methods (total variation and non-convex estimators) replace the least-squares estimator by another one, assumed to be robust to discontinuities. Yet, it is possible to proceed differently: the 1D-graph in figure 5 shows that most data are corrupted only by noise, and that the discontinuity set is “small”. Hence, applying least-squares everywhere except on this set should provide an optimal 3D-reconstruction. To achieve this, a first possibility is to consider weighted least-squares:

$$\min_z \iint_{(u,v) \in \Omega} \|\mathbf{W}(u,v) [\nabla z(u,v) - \mathbf{g}(u,v)]\|^2 + \lambda(u,v) [z(u,v) - z^0(u,v)]^2 du dv \quad (74)$$

where \mathbf{W} is a $\Omega \rightarrow \mathbb{R}^{2 \times 2}$ tensor field, acting as a weight map designed to reduce the influence of discontinuity points. The weights can be a priori computed according to the integrability of \mathbf{g} [48], or by convolution of the components of \mathbf{g} by a Gaussian kernel [1]. Yet, such approaches are of limited interest when \mathbf{g} contains noise. In this case, the weights should rather be set as a function inversely proportional to $\|\nabla z(u,v)\|$, e.g.:

$$\mathbf{W}(u,v) = \frac{1}{\sqrt{\left(\frac{\|\nabla z(u,v)\|}{\mu}\right)^2 + 1}} \mathbf{I}_2 \quad (75)$$

with μ a user-defined hyper-parameter. The latter tensor is the one proposed by Perona and Malik in [45]: the continuous optimality condition associated to (74) is related to their “anisotropic diffusion model”⁷. Such tensor fields $\mathbf{W} : \Omega \rightarrow \mathbb{R}^{2 \times 2}$ are called “diffusion tensors”: we refer the reader to [54] for a complete overview.

The use of diffusion tensors for the integration problem is not new [48], but we provide hereafter additional comments on the statistical interpretation of such tensors. Interestingly, the diffusion tensor (75) also appears when making different assumptions on the noise model than those we considered so far. Up to now, we assumed that the input gradient field \mathbf{g} was equal to the gradient ∇z of the depth map z , up to an additive, zero-mean, Gaussian noise: $\mathbf{g} = \nabla z + \epsilon$, $\epsilon \sim \mathcal{N}\left([0, 0]^\top, \begin{bmatrix} \sigma^2 & 0 \\ 0 & \sigma^2 \end{bmatrix}\right)$. This hypothesis may not always be realistic. For instance, in 3D-reconstruction scenarii such as photometric stereo [55], one estimates the normal field $\mathbf{n} : \Omega \rightarrow \mathbb{R}^3$ pixelwise, rather than the gradient $\mathbf{g} : \Omega \rightarrow \mathbb{R}^2$, from a set of images. Hence, the Gaussian assumption should rather be made on these images. In this case, and provided that a maximum-likelihood for the normals is used, it may be assumed that the estimated normal field is the genuine one, up to an additive Gaussian noise. Yet, this does not imply that the noise in the gradient field \mathbf{g} is Gaussian-distributed. Let us clarify this point.

Assuming orthographic projection, the relationship between \mathbf{n} and ∇z is written, at every point (u,v) where the depth map z is differentiable:

$$\mathbf{n}(u,v) = \frac{1}{\sqrt{\|\nabla z(u,v)\|^2 + 1}} [-\nabla z(u,v)^\top, 1]^\top \quad (76)$$

which implies that $[-\frac{n_1}{n_3}, -\frac{n_2}{n_3}]^\top = [\partial_u z, \partial_v z]^\top = \nabla z$. If we denote $\bar{\mathbf{n}}$ the estimated normal field, it also follows from (76) that $[-\frac{\bar{n}_1}{\bar{n}_3}, -\frac{\bar{n}_2}{\bar{n}_3}]^\top = [p, q]^\top = \mathbf{g}$.

⁷ Although (75) actually yields an isotropic diffusion model, since it “utilizes a scalar-valued diffusivity and not a diffusion tensor” [54].

Let us assume that $\bar{\mathbf{n}}$ and \mathbf{n} differ according to an additive, zero-mean, Gaussian noise:

$$\bar{\mathbf{n}}(u, v) = \mathbf{n}(u, v) + \boldsymbol{\epsilon}(u, v) \quad (77)$$

where :

$$\boldsymbol{\epsilon}(u, v) \sim \mathcal{N} \left([0, 0, 0]^\top, \begin{bmatrix} \sigma^2 & 0 & 0 \\ 0 & \sigma^2 & 0 \\ 0 & 0 & \sigma^2 \end{bmatrix} \right) \quad (78)$$

Since \bar{n}_3 is unlikely to take negative values (this would mean that the estimated surface is not oriented towards the camera), the following Geary-Hinkley transforms:

$$t_1 = \frac{n_3 \left(\frac{\bar{n}_1}{\bar{n}_3} \right) - n_1}{\sqrt{\sigma^2 \left(\left(\frac{\bar{n}_1}{\bar{n}_3} \right)^2 + 1 \right)}} \quad (79)$$

$$t_2 = \frac{n_3 \left(\frac{\bar{n}_2}{\bar{n}_3} \right) - n_2}{\sqrt{\sigma^2 \left(\left(\frac{\bar{n}_2}{\bar{n}_3} \right)^2 + 1 \right)}} \quad (80)$$

both follow standard Gaussian distribution $\mathcal{N}(0, 1)$ [28]. After some algebra, this can be rewritten as:

$$\frac{1}{\sigma \sqrt{1 + p^2} \sqrt{\|\nabla z\|^2 + 1}} [\partial_u z - p] \sim \mathcal{N}(0, 1) \quad (81)$$

$$\frac{1}{\sigma \sqrt{1 + q^2} \sqrt{\|\nabla z\|^2 + 1}} [\partial_v z - q] \sim \mathcal{N}(0, 1) \quad (82)$$

This rationale suggests the use of the following fidelity term:

$$\mathcal{F}_{\text{PM}}(z) = \iint_{(u,v) \in \Omega} \|\mathbf{W}(u, v) [\nabla z(u, v) - \mathbf{g}(u, v)]\|^2 du dv \quad (83)$$

where $\mathbf{W}(u, v)$ is the following 2×2 anisotropic diffusion tensor field:

$$\mathbf{W}(u, v) = \frac{1}{\sqrt{\|\nabla z(u, v)\|^2 + 1}} \begin{bmatrix} \frac{1}{\sqrt{1+p(u,v)^2}} & 0 \\ 0 & \frac{1}{\sqrt{1+q(u,v)^2}} \end{bmatrix} \quad (84)$$

Unfortunately, we experimentally found that choosing (84) for the diffusion tensor field, discontinuities were not always recovered. Instead, following the pioneering ideas from Perona and Malik [45], we introduce two parameters μ and ν to control the respective influences of the terms forming the tensor field:

$$\mathbf{W}(u, v) = \frac{1}{\sqrt{\left(\frac{\|\nabla z(u, v)\|}{\mu} \right)^2 + 1}} \begin{bmatrix} \frac{1}{\sqrt{1+\left(\frac{p(u,v)}{\nu}\right)^2}} & 0 \\ 0 & \frac{1}{\sqrt{1+\left(\frac{q(u,v)}{\nu}\right)^2}} \end{bmatrix} \quad (85)$$

Replacing the matrix in (85) by \mathbf{I}_2 yields exactly the Perona-Malik diffusion tensor (75), which reduces the influence of the fidelity term on locations (u, v) where $\|\nabla z(u, v)\|$ increases, which are likely to indicate discontinuities. Yet, our diffusion tensor (85) also reduces the influence of points where p or q is high, which are also likely to correspond to discontinuities. In our experiments, we found that $\nu = 10$ could always be used, yet the choice of μ has more influence on the actual results.

Discretization. Using the same discretization strategy as in subsections 3.2 and 3.3 leads us to the following discrete functional:

$$E_{\text{PM}}(\mathbf{z}) = \frac{1}{4} \sum_{(U,V) \in \{+,-\}^2} \sum_{(U,V) \in \{+,-\}^2} \left\{ \|\mathbf{A}^{UV}(\mathbf{z}) (\mathbf{D}_u^U \mathbf{z} - \mathbf{p})\|^2 + \|\mathbf{B}^{UV}(\mathbf{z}) (\mathbf{D}_v^V \mathbf{z} - \mathbf{q})\|^2 + \|\mathbf{A}(\mathbf{z} - \mathbf{z}^0)\|^2 \right\} \quad (86)$$

where the $\mathbf{A}^{UV}(\mathbf{z})$ and $\mathbf{B}^{UV}(\mathbf{z})$ are $|\Omega| \times |\Omega|$ diagonal matrices containing the following $\{a_{u,v}^{UV}\}$ and $\{b_{u,v}^{UV}\}$ values, $(u, v) \in \Omega$:

$$a_{u,v}^{UV} = \frac{1}{\sqrt{1 + \left(\frac{p_{u,v}}{\nu}\right)^2} \sqrt{\frac{(\partial_u^U z_{u,v})^2 + (\partial_v^V z_{u,v})^2}{\mu^2} + 1}} \quad (87)$$

$$b_{u,v}^{UV} = \frac{1}{\sqrt{1 + \left(\frac{q_{u,v}}{\nu}\right)^2} \sqrt{\frac{(\partial_u^U z_{u,v})^2 + (\partial_v^V z_{u,v})^2}{\mu^2} + 1}} \quad (88)$$

with $(U, V) \in \{+, -\}^2$.

Numerical resolution. Since the coefficients $a_{u,v}^{UV}$ and $b_{u,v}^{UV}$ depend in a nonlinear way on the unknown values $z_{u,v}$, it is difficult to derive a closed-form expression for the minimizer of (86). To deal with this issue, we use the following fixed point scheme, which iteratively updates the anisotropic diffusion tensors and the z -values:

$$\mathbf{z}^{(k+1)} = \underset{\mathbf{z} \in \mathbb{R}^{|\Omega|}}{\text{argmin}} \frac{1}{4} \sum_{(U,V) \in \{+,-\}^2} \sum_{(U,V) \in \{+,-\}^2} \left\{ \|\mathbf{A}^{UV}(\mathbf{z}^{(k)}) (\mathbf{D}_u^U \mathbf{z} - \mathbf{p})\|^2 + \|\mathbf{B}^{UV}(\mathbf{z}^{(k)}) (\mathbf{D}_v^V \mathbf{z} - \mathbf{q})\|^2 + \|\mathbf{A}(\mathbf{z} - \mathbf{z}^0)\|^2 \right\} \quad (89)$$

Now that the diffusion tensor coefficients are fixed, each optimization problem (89) is reduced to a simple linear least-squares problem. In our implementation, we solve the corresponding optimality condition using Cholesky factorization, which we experimentally found to provide more stable results than conjugate gradient iterations.

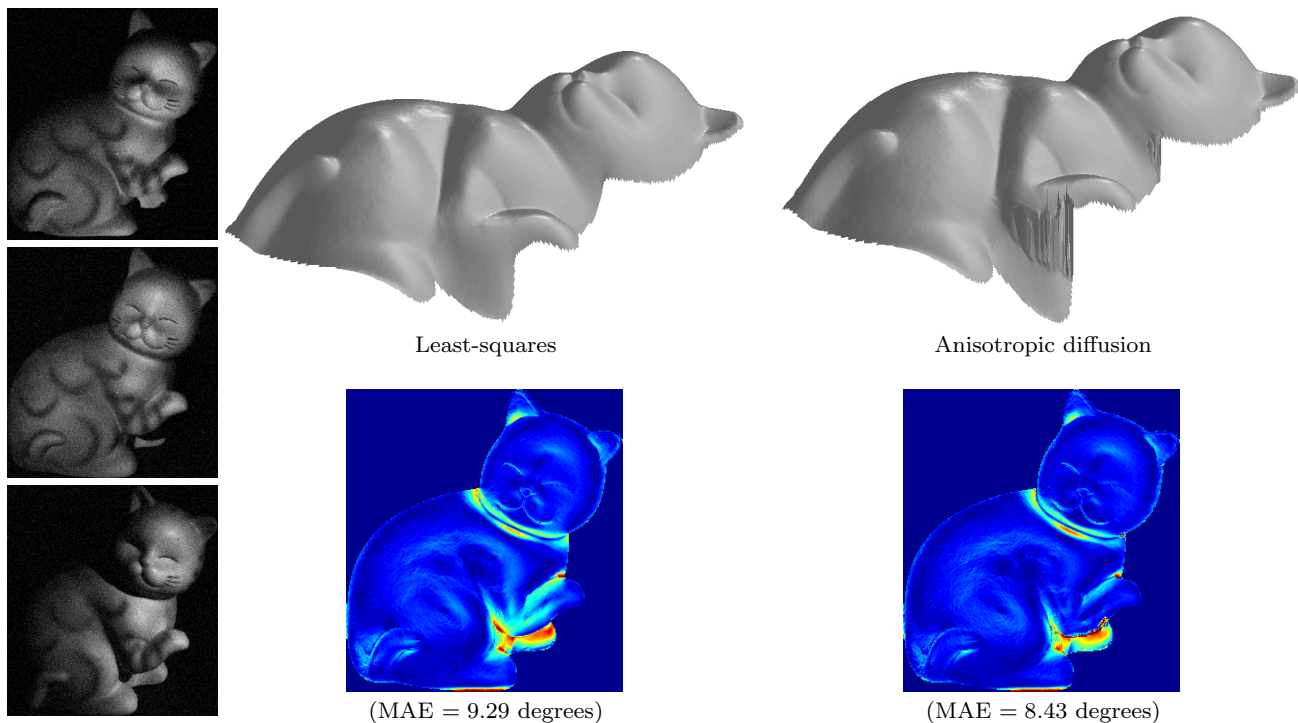


Fig. 10 Left: three out of the 96 input images used for estimating the normals by photometric stereo [55]. Center: 3D-reconstruction by least-squares integration of the normals (section 2), and angular error map (blue is 0 degree, red is 60 degrees). The estimation is biased around the occluded areas. Right: same, using anisotropic diffusion integration with the tensor field defined in (84). The errors remain confined in the occluded parts, and do not propagate over the discontinuities.

Discussion. We first experimentally verify that the proposed anisotropic diffusion approach is indeed a statistically meaningful approach in the context of photometric stereo. As stated in [40], “in previous work on photometric stereo, noise is [wrongly] added to the gradient of the height function rather than camera images”. Hence, we consider the images from the “Cat” dataset presented in [52], and add a zero-mean, Gaussian noise with standard deviation $\sigma \|I\|_\infty$, $\sigma = 5\%$, to the images, where $\|I\|_\infty$ is the maximum graylevel value. The normals were computed by photometric stereo [55] over the part representing the cat. Then, since only the ground-truth normals are provided in [52], and not the depth map, we a posteriori computed the final normal maps by central finite differences. This allows us to calculate the angular error, in degrees, between the real surface and the reconstructed one. The mean angular error (MAE) can eventually be computed over the set of pixels for which central finite differences make sense (boundary and background points are excluded).

Figure 10 shows that the 3D-reconstruction obtained by anisotropic diffusion outperforms that obtained by least-squares. Besides, although we used the diffusion tensor (84) (which does not require any parameter tuning), discontinuities are partially recovered. The superiority of anisotropic diffusion over least-squares remains

true when increasing the amount of noise (cf. figure 11), which clearly indicates that the anisotropic diffusion approach is indeed better-suited for dealing with noise on the images. Yet, the restoration of discontinuities is not as sharp as with the previous approaches, and artifacts are visible along the discontinuities (cf. figure 10).

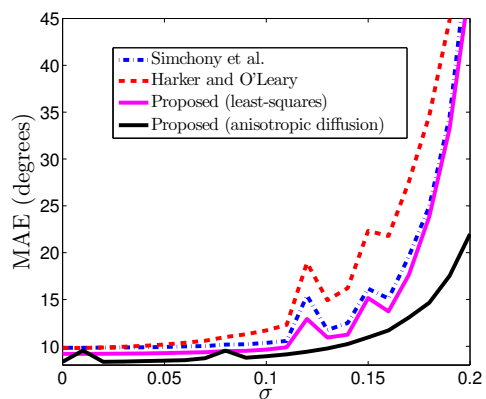


Fig. 11 Mean angular error (in degrees) as a function of the standard deviation $\sigma \|I\|_\infty$ of the noise which was added to the photometric stereo images. The anisotropic diffusion approach always outperforms least-squares. For the methods of Simchony et al. [53] and Harker and O’Leary [27], the gradient field was filled with zeros outside the reconstruction domains, which adds even more bias.

Although the parameter-free diffusion tensor (84) seems able to recover discontinuities, this is not always the case. For instance, we did not succeed in recovering the discontinuities of the surface $\mathcal{S}_{\text{vase}}$. For this dataset, we had to use the tensor (85). The results from figure 12 show that with an appropriate tuning of μ , discontinuities are recovered and Gibbs phenomena are removed, without staircasing artifact. Yet, as in the experiment of figure 10, the discontinuities are not very sharp. Such artifacts were also observed by Badri et al. [4], when experimenting with the anisotropic diffusion tensor from Agrawal et al. [1]. Sharper discontinuities could be recovered by using binary weights: this is the spirit of the Mumford-Shah segmentation method, which we explore in the next subsection.

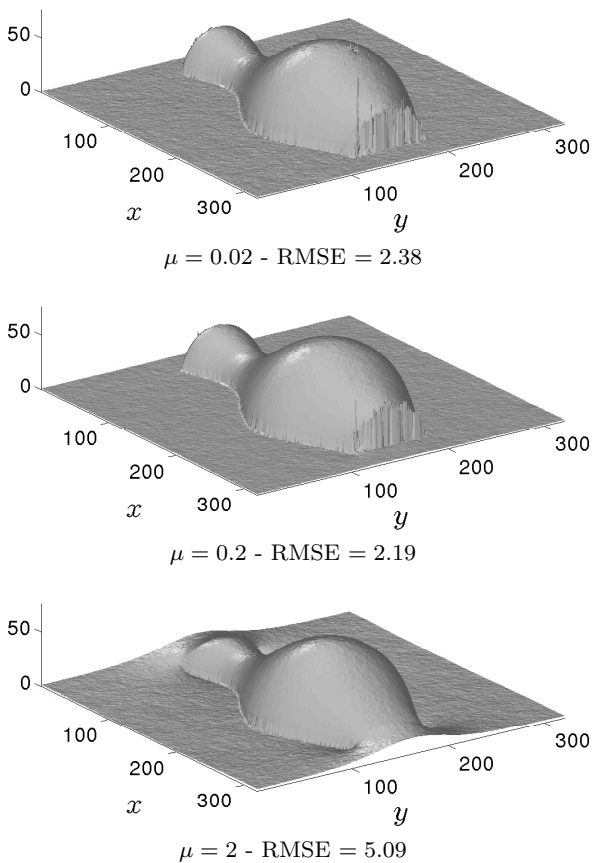


Fig. 12 Integration by anisotropic diffusion. As long as μ is small enough, discontinuities are recovered. Besides, no staircasing artifact is visible. Yet, the restored discontinuities are not perfectly sharp.

3.5 Adaptation of the Mumford and Shah Functional

Let $z^0 : \Omega \rightarrow \mathbb{R}$ be a noisy image to restore. In order to estimate a denoised image z while perserving the discontinuities of the original image, Mumford and Shah suggested in [38] to minimize a quadratic functional only over a subset $\Omega \setminus K$ of Ω , while automatically estimating the discontinuity set K according to some prior. A reasonable prior is that K must be “small”, so that its length can be penalized, leading to the following optimization problem:

$$\begin{aligned} \min_{z, K} \quad & \mu \iint_{(u,v) \in \Omega \setminus K} \|\nabla z(u, v)\|^2 du dv + \int_K d\sigma \\ & + \lambda \iint_{(u,v) \in \Omega \setminus K} [z(u, v) - z^0(u, v)]^2 du dv \end{aligned} \quad (90)$$

where λ and μ are positive constants, and $\int_K d\sigma$ is the length of the set K (which models the discontinuities in the image). We refer the reader to [3] for a detailed introduction about this model and its qualitative properties.

Several approaches have been proposed to numerically minimize the Mumford-Shah functional: finite differences scheme [11], piecewise constant approximation [13], primal-dual algorithms [47], etc. Another approach consists in using elliptic functionals. An auxiliary function $w : \Omega \rightarrow \mathbb{R}$ is introduced. This function stands for $1 - \chi_K$, where χ_K is the characteristic function of the set K . Ambrosio and Tortorelli have proposed in [2] to consider the following optimization problem:

$$\begin{aligned} \min_{z, w} \quad & \mu \iint_{(u,v) \in \Omega} w(u, v)^2 \|\nabla z(u, v)\|^2 du dv \\ & + \iint_{(u,v) \in \Omega} \left[\epsilon \|\nabla w(u, v)\|^2 + \frac{1}{4\epsilon} [w(u, v) - 1]^2 \right] du dv \\ & + \lambda \iint_{(u,v) \in \Omega} [z(u, v) - z^0(u, v)]^2 du dv \end{aligned} \quad (91)$$

By using the theory of Γ -convergence, it is possible to show that (91) is a way to solve (90) when $\epsilon \rightarrow 0$.

We modify the above models, so that they fit our integration problem. Considering \mathbf{g} as basis for least-squares integration everywhere except on the discontinuity set K , we obtain the following energy:

$$\begin{aligned} \mathcal{E}_{\text{MS}}(z, K) = \quad & \mu \iint_{(u,v) \in \Omega \setminus K} \|\nabla z(u, v) - \mathbf{g}(u, v)\|^2 du dv + \int_K d\sigma \\ & + \iint_{(u,v) \in \Omega \setminus K} \lambda(u, v) [z(u, v) - z^0(u, v)]^2 du dv \end{aligned} \quad (92)$$

for the Mumford-Shah functional, while the approach by elliptic functionals leads us to replace (92) by the Ambrosio-Tortorelli approximation:

$$\begin{aligned} \mathcal{E}_{\text{AT}}(z, w) &= \mu \iint_{(u,v) \in \Omega} w(u, v)^2 \|\nabla z(u, v) - \mathbf{g}(u, v)\|^2 du dv \\ &+ \iint_{(u,v) \in \Omega} \left[\epsilon \|\nabla w(u, v)\|^2 + \frac{1}{4\epsilon} [w(u, v) - 1]^2 \right] du dv \\ &+ \iint_{(u,v) \in \Omega} \lambda(u, v) [z(u, v) - z^0(u, v)]^2 du dv \end{aligned} \quad (93)$$

where $w : \Omega \rightarrow \mathbb{R}$ is a smooth approximation of $1 - \chi_K$.

Numerical resolution. We use the same strategy as in section 2 for discretizing $\nabla z(u, v)$ inside functional (93), i.e. all the possible first-order discrete approximations of the differential operators are summed. Since discontinuities are usually “thin” structures, it is possible that a forward discretization contains the discontinuity while a backward discretization does not. Hence, the definition of the weights w should be made accordingly to that of ∇z . Thus, we define four fields $w_{u/v}^{+/-} : \Omega \rightarrow \mathbb{R}$, associated with the finite differences operators $\partial_{u/v}^{+/-}$. This leads to the following discrete analogous of functional (93):

$$\begin{aligned} E_{\text{AT}}(\mathbf{z}, \mathbf{w}_u^+, \mathbf{w}_u^-, \mathbf{w}_v^+, \mathbf{w}_v^-) &= \\ &+ \frac{\mu}{2} \left(\|\mathbf{W}_u^+ (\mathbf{D}_u^+ \mathbf{z} - \mathbf{p})\|^2 + \|\mathbf{W}_u^- (\mathbf{D}_u^- \mathbf{z} - \mathbf{p})\|^2 \right. \\ &\quad \left. + \|\mathbf{W}_v^+ (\mathbf{D}_v^+ \mathbf{z} - \mathbf{q})\|^2 + \|\mathbf{W}_v^- (\mathbf{D}_v^- \mathbf{z} - \mathbf{q})\|^2 \right) \\ &+ \frac{\epsilon}{2} \left(\|\mathbf{D}_u^+ \mathbf{w}_u^+\|^2 + \|\mathbf{D}_u^- \mathbf{w}_u^-\|^2 + \|\mathbf{D}_v^+ \mathbf{w}_v^+\|^2 + \|\mathbf{D}_v^- \mathbf{w}_v^-\|^2 \right) \\ &+ \frac{1}{8\epsilon} \left(\|\mathbf{w}_u^+ - \mathbf{1}\|^2 + \|\mathbf{w}_u^- - \mathbf{1}\|^2 + \|\mathbf{w}_v^+ - v\mathbf{1}\|^2 + \|\mathbf{w}_v^- - \mathbf{1}\|^2 \right) \\ &+ \|\mathbf{A} (\mathbf{z} - \mathbf{z}^0)\|^2 \end{aligned} \quad (94)$$

where $\mathbf{w}_{u/v}^{+/-} \in \mathbb{R}^{|\Omega|}$ is a vector containing the values of the discretized field $w_{u/v}^{+/-}$, and $\mathbf{W}_{u/v}^{+/-} = \text{Diag}(\mathbf{w}_{u/v}^{+/-})$ is the $|\Omega| \times |\Omega|$ diagonal matrix containing these values.

We tackle the nonlinear problem (94) by an alternating optimization scheme:

$$\mathbf{z}^{(k+1)} = \underset{\mathbf{z} \in \mathbb{R}^{|\Omega|}}{\text{argmin}} E_{\text{AT}}(\mathbf{z}, \mathbf{w}_u^{+(k)}, \mathbf{w}_u^{-(k)}, \mathbf{w}_v^{+(k)}, \mathbf{w}_v^{-(k)}) \quad (95)$$

$$\mathbf{w}_u^{+(k+1)} = \underset{\mathbf{w} \in \mathbb{R}^{|\Omega|}}{\text{argmin}} E_{\text{AT}}(\mathbf{z}^{(k+1)}, \mathbf{w}, \mathbf{w}_u^{-(k)}, \mathbf{w}_v^{+(k)}, \mathbf{w}_v^{-(k)}) \quad (96)$$

and similar straightforward updates for the other indicator functions. We can choose as initial guess, for

instance, the smooth solution from section 2 for $\mathbf{z}^{(0)}$, and $\mathbf{w}_u^{+(0)} = \mathbf{w}_u^{-(0)} = \mathbf{w}_v^{+(0)} = \mathbf{w}_v^{-(0)} \equiv \mathbf{1}$.

At each iteration (k), updating the surface and the indicator functions requires solving a series of linear least-squares problems. We achieve this by solving the resulting linear systems (normal equations) by means of the conjugate gradient algorithm. Contrarily to the approaches that we presented so far, the matrices involved in these systems are modified at each iteration. Hence, it is not possible to compute the preconditioner beforehand. It could be computed at each iteration, but in our experiments we did not consider any preconditioning strategy at all. Thus, the proposed scheme could obviously be accelerated. For instance, it might be interesting to propose a strategy for iteratively refining the preconditioner, rather than not using any or fully computing it at each iteration. This is left as perspective.

Discussion. Let us now check experimentally, on the same noisy gradient of surface $\mathcal{S}_{\text{vase}}$ as in previous experiments, whether this new integration method, inspired by the Mumford-Shah functional, satisfies the expected properties. In the experiment of figure 13, we performed 50 iterations of the proposed alternating optimization scheme, with various choices for the hyperparameter μ . The ϵ parameter was set to $\epsilon = 0.1$ (we recall that this parameter is not critical: it only has to be “small enough”, in order for the Ambrosio-Tortorelli approximation to converge towards the Mumford-Shah functional). As it was already the case with other non-convex regularizers (cf. subsection 3.3), a bad tuning of the parameter leads either to over-smoothing (high values of μ) or to staircasing artifacts (low values of μ), which indicate the presence of local minima. Yet, by appropriately setting this parameter, we obtain a 3D-reconstruction which is very close to the genuine surface, without staircasing artifact.

The Mumford-Shah functional being non-convex, local minima may be present. Yet, as shown in figure 14, the choice of the initialization may not be as crucial as with the non-convex estimators from subsection 3.3. Indeed, the 3D-reconstruction of the “Canadian tent” surface, using as initial guess the least-squares solution, is similar to that obtained by using the trivial initialization $\mathbf{z}^{(0)} \equiv 0$.

Hence, among the methods we have studied, the adaptation of the Mumford-Shah model is the approach which provides the most satisfactory 3D-reconstructions: it is possible to recover sharp discontinuities, even in the presence of noise, and with limited artifacts.

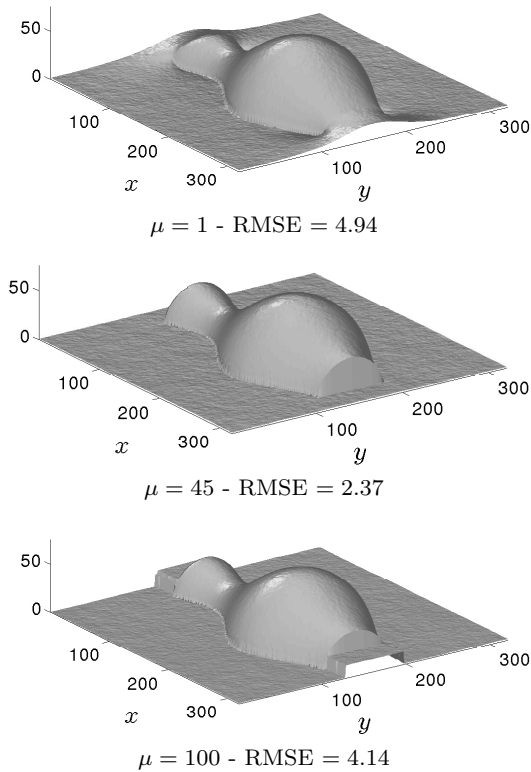


Fig. 13 3D-reconstructions from the noisy gradient of $\mathcal{S}_{\text{vase}}$, using the Mumford-Shah integrator. If μ is tuned appropriately, sharp discontinuities can be restored, without staircasing artifacts.

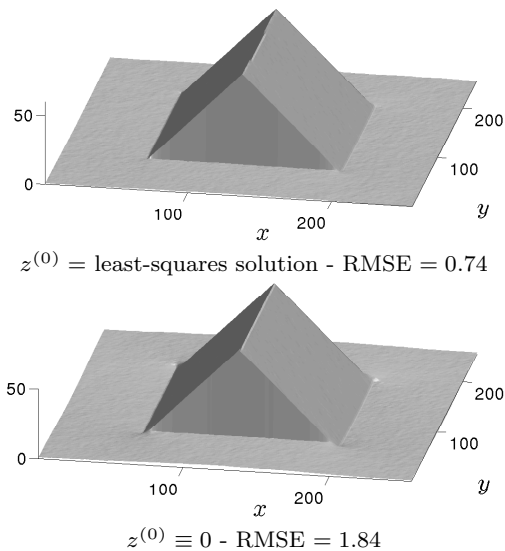


Fig. 14 3D-reconstruction of the “Canadian tent” surface by the Mumford-Shah integrator ($\mu = 20$), using two different initializations. The choice of the initial guess matters, but not as much as with the non-convex estimators from section 3.3.

4 Conclusion and Perspectives

We presented a thorough review of the state-of-the-art in a first paper (Part I: A Survey), as well as new methods for integrating a dense gradient field in the present one (Part II: New Insights). The review allowed us to select six criteria which should be met by an optimal integration method: $\mathcal{P}_{\text{Fast}}$, $\mathcal{P}_{\text{Robust}}$, $\mathcal{P}_{\text{FreeB}}$, $\mathcal{P}_{\text{Disc}}$, $\mathcal{P}_{\text{NoPar}}$ and $\mathcal{P}_{\text{NoRect}}$. We then detailed in section 2 a least-squares solution designed to meet all these criteria, except $\mathcal{P}_{\text{Disc}}$. Eventually, we discussed in section 3 several non-quadratic or non-convex variational formulations. Although these approaches are slower and a parameter must be tuned, they are able to recover sharp features such as discontinuities and kinks ($\mathcal{P}_{\text{Disc}}$ is satisfied).

Among these methods, which are summarized in table 1, we believe that the Mumford-Shah approach discussed in section 3.5 is the one which represents the overall best compromise. Yet, the other ones are also promising. Indeed, other non-convex estimators than those introduced in section 3.3 may create less staircasing, and other anisotropic diffusion tensors than those proposed in section 3.4 may yield reduced artifacts.

Future research directions may include accelerating the numerical schemes and proving their convergence when this is not trivial (e.g., for the non-convex integrators). We also believe that introducing additional smoothness terms inside the functionals may be useful for eliminating the artifacts in anisotropic diffusion integration. Quadratic (Tikhonov) smoothness terms were suggested in [27]: to enforce surface smoothness while preserving the discontinuities, we should rather consider non-quadratic ones. In this view, higher-order functionals (e.g., total generalized variation methods [8]) may reduce not only these artifacts, but also staircasing. Indeed, as shown in figure 15, such artifacts may be visible when performing photometric stereo [55] without prior segmentation. Yet, this example also shows that the artifacts are visible only over the background, and do not seem to affect the relevant part.

3D-reconstruction is not the only application where efficient tools for gradient field integration are required. Although the assumption on the noise distribution may differ from one application to another, PDE-based imaging problems such as Laplace image compression [46] or Poisson image editing [44] also require an efficient integrator. In this view, the ability of our methods to handle control points may be useful. We illustrate in figure 16 an interesting application. From an RGB image I , we selected the points where the norm of the gradient of the luminance was the highest (conserving only 10% of the points). Then, we created a gradient field \mathbf{g} equal to zero everywhere, except on the control points, where

Table 1 Main features of the five methods of integration proposed in this paper. The quadratic method has all desirable properties, except $\mathcal{P}_{\text{Disc}}$. The others hold $\mathcal{P}_{\text{Disc}}$ (*: except the total variation approach in the presence of noise), yet they lose $\mathcal{P}_{\text{Fast}}$. In addition, all discontinuity-preserving methods except TV require tuning at least one hyper-parameter. Besides, staircasing artifacts may appear. Overall, despite such artifacts, we recommend the Mumford-Shah approach, using the quadratic method as initial guess, in order to avoid local minima.

Method	$\mathcal{P}_{\text{Fast}}$	$\mathcal{P}_{\text{Robust}}$	$\mathcal{P}_{\text{FreeB}}$	$\mathcal{P}_{\text{Disc}}$	$\mathcal{P}_{\text{NoRect}}$	$\mathcal{P}_{\text{NoPar}}$	Local minima	Staircasing
Quadratic	+	+	+	-	+	+	No	No
Total variation	-	+	+	+	+	+	No	Yes
Non-convex	-	+	+	+	+	-	Yes	Yes
Anisotropic diffusion	-	+	+	+	+	-	No	No
Mumford-Shah	-	+	+	+	+	-	Yes	Yes

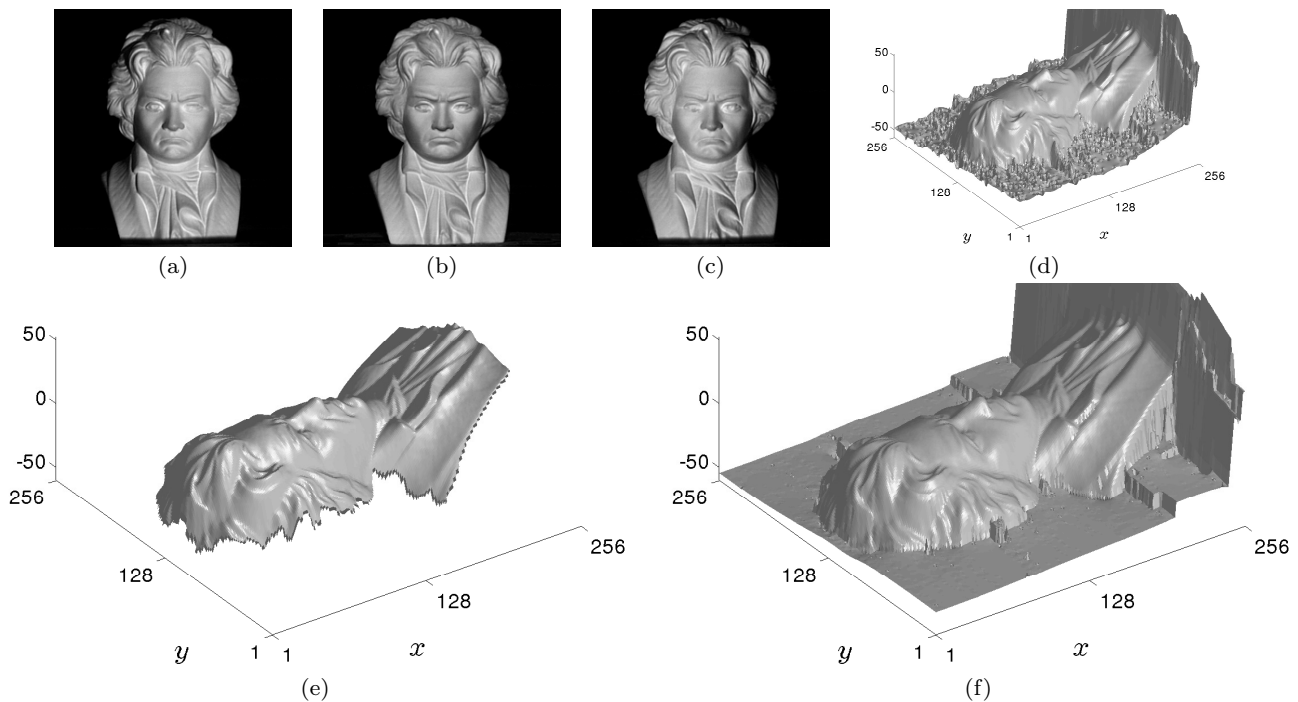


Fig. 15 3D-reconstruction using photometric stereo. (a-c) All (real) input images. (d) 3D-reconstruction by least-squares, without segmentation. (e) 3D-reconstruction by least-squares, after segmentation. (f) 3D-reconstruction using the Mumford-Shah approach, without segmentation. When discontinuities are handled, it is possible to perform photometric stereo without prior segmentation of the object.

it was set to the gradient of the color levels. The prior z^0 was set to a null scalar field, except on the control points where we retained the original color data. Eventually, λ is set to an arbitrary small value ($\lambda = 10^{-9}$) everywhere, except on the control points ($\lambda = 10$). The integration of each color channel gradient is performed independently, using the Mumford-Shah method to extrapolate the data from the control points to the whole grid. Using this approach, we obtain a nice piecewise-constant approximation of the image, in the spirit of the “texture-flattening” application presented in [44]. Besides, by selecting the control points in a more optimal way [6, 29], this approach could easily be extended to image compression, reaching state-of-the-art lossy

compression rates. In fact, existing PDE-based methods can already compete with the compression rate of the well-known JPEG 2000 algorithm [46]. We believe that the proposed edge-preserving framework may yield even better results.

Eventually, some of the research directions already mentioned in the conclusion section of our first paper were ignored in this second paper, but they remain of important interest. One of the most appealing examples is multi-view normal field integration [14]. Indeed, discontinuities represent a difficulty in our case because they are induced by occlusions, yet more information would be obtained near the occluding contours by using additional views.

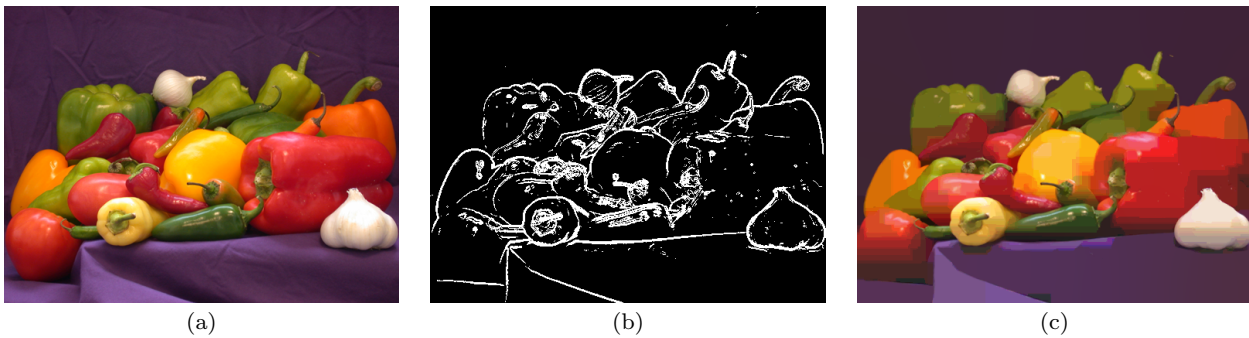


Fig. 16 Application to image compression/image editing. (a) Reference image. (b) Control points (where the RGB-values and their gradients are kept). (c) Restored image obtained by considering the proposed Mumford-Shah integrator as a piecewise-constant interpolation method. A reasonable piecewise constant restoration of the initial image can be obtained from as few as 10% of the initial information.

References

1. Agrawal, A., Raskar, R., Chellappa, R.: What Is the Range of Surface Reconstructions from a Gradient Field? In: Proceedings of the 9th European Conference on Computer Vision (volume I), *Lecture Notes in Computer Science*, vol. 3951, pp. 578–591. Graz, Austria (2006) [6](#), [8](#), [16](#), [19](#)
2. Ambrosio, L., Tortorelli, V.M.: Approximation of Functionals Depending on Jumps by Elliptic Functionals via Γ -convergence. *Communications in Pure and Applied Mathematics* **43**, 999–1036 (1990) [19](#)
3. Aubert, G., Kornprobst, P.: Mathematical Problems in Image Processing, *Applied Mathematical Sciences*, vol. 147. Springer-Verlag (2002) [2](#), [14](#), [19](#)
4. Badri, H., Yahia, H., Aboutajdine, D.: Robust Surface Reconstruction via Triple Sparsity. In: IEEE Conference on Computer Vision and Pattern Recognition (CVPR), pp. 2291–2298. Columbus, USA (2014) [14](#), [19](#)
5. Beck, A., Teboulle, M.: A Fast Iterative Shrinkage-Thresholding Algorithm for Linear Inverse Problems. *SIAM Journal on Imaging Sciences* **2**(1), 183–202 (2009) [13](#)
6. Belhachmi, B., Bucur, D., Burgeth, B., Weickert, J.: How to Choose Interpolation Data in Images. *SIAM Journal on Applied Mathematics* **70**(1), 333–352 (2009) [22](#)
7. Boyd, S., Parikh, N., Chu, E., Peleato, B., Eckstein, J.: Distributed Optimization and Statistical Learning via the Alternating Direction Method of Multipliers. *Foundations and Trends in Machine Learning* **3**(1), 1–122 (2011) [12](#)
8. Bredies, K., Holler, M.: A TGV-Based Framework for Variational Image Decompression, Zooming, and Reconstruction. Part I: Analytics. *SIAM Journal on Imaging Sciences* **8**(4), 2814–2850 (2015) [13](#), [21](#)
9. Breuss, M., Quéau, Y., Bähr, M., Durou, J.D.: Highly Efficient Surface Normal Integration. In: Proceedings of the Algorithm Conference on Scientific Computing (2016) [4](#), [6](#)
10. Catte, F., Lions, P.L., Morel, J.M., Coll, T.: Image Selective Smoothing and Edge Detection by Nonlinear Diffusion. *SIAM Journal on Numerical Analysis* **29**(1), 182–193 (1992) [2](#)
11. Chambolle, A.: Image Segmentation by Variational Methods: Mumford and Shah Functional and the Discrete Approximation. *SIAM Journal of Applied Mathematics* **55**(3), 827–863 (1995) [19](#)
12. Chambolle, A., Pock, T.: A First-Order Primal-Dual Algorithm for Convex Problems with Applications to Imaging. *Journal of Mathematical Imaging and Vision* **40**(1), 120–145 (2010) [2](#), [13](#)
13. Chan, T.F., Vese, L.A.: Active Contours Without Edges. *IEEE Transactions on Image Processing* **10**(2), 266–277 (2001) [19](#)
14. Chang, J.Y., Lee, K.M., Lee, S.U.: Multiview Normal Field Integration Using Level Set Methods. In: Proceedings of the IEEE Conference on Computer Vision and Pattern Recognition, Workshop on Beyond Multiview Geometry: Robust Estimation and Organization of Shapes from Multiple Cues. Minneapolis, Minnesota, USA (2007) [22](#)
15. Charbonnier, P., Blanc-Féraud, L., Aubert, G., Barlaud, M.: Deterministic Edge-Preserving Regularization in Computed Imaging. *IEEE Transactions on Image Processing* **6**(2), 298–311 (1997) [2](#)
16. Chen, S.S., Donoho, D.L., Saunders, M.A.: Atomic Decomposition by Basis Pursuit. *SIAM Journal on Scientific Computing* **20**(1), 33–61 (1998) [13](#)
17. Du, Z., Robles-Kelly, A., Lu, F.: Robust Surface Reconstruction from Gradient Field Using the L1 Norm. In: Proceedings of the 9th Biennial Conference of the Australian Pattern Recognition Society on Digital Image Computing Techniques and Applications, pp. 203–209. Glenelg, Australia (2007) [12](#)
18. Durou, J.D., Aujol, J.F., Courteille, F.: Integration of a Normal Field in the Presence of Discontinuities. In: Proceedings of the 7th International Workshop on Energy Minimization Methods in Computer Vision and Pattern Recognition, *Lecture Notes in Computer Science*, vol. 5681, pp. 261–273. Bonn, Germany (2009) [1](#), [3](#), [14](#)
19. Durou, J.D., Aujol, J.F., Quéau, Y.: Normal Integration – Part I: A Survey. *Journal of Mathematical Imaging and Vision* (2016). (submitted) [1](#), [3](#), [4](#), [9](#), [10](#)
20. Durou, J.D., Courteille, F.: Integration of a Normal Field without Boundary Condition. In: Proceedings of the 11th IEEE International Conference on Computer Vision, 1st Workshop on Photometric Analysis for Computer Vision. Rio de Janeiro, Brazil (2007) [1](#), [2](#), [3](#), [4](#), [6](#)
21. Frankot, R.T., Chellappa, R.: A Method for Enforcing Integrability in Shape from Shading Algorithms. *IEEE Transactions on Pattern Analysis and Machine Intelligence* **10**(4), 439–451 (1988) [6](#)
22. Gabay, D., Mercier, B.: A dual algorithm for the solution of nonlinear variational problems via finite element

- approximation. *Computers & Mathematics with Applications* **2**(1), 17 – 40 (1976) [12](#)
23. Geman, D., Reynolds, G.: Constrained Restoration and Recovery of Discontinuities. *IEEE Transactions on Pattern Analysis and Machine Intelligence* **14**(3), 367–383 (1992) [2](#)
 24. Goldstein, T., O’Donoghue, B., Setzer, S., Baraniuk, R.: Fast Alternating Direction Optimization Methods. *SIAM Journal on Imaging Sciences* **7**(3), 1588–1623 (2014) [2](#), [13](#)
 25. Goldstein, T., Osher, S.: The split Bregman method for L1-regularized problems. *SIAM Journal on Imaging Sciences* **2**(2), 323–343 (2009) [12](#)
 26. Haque, S.M., Chatterjee, A., Govindu, V.M.: High Quality Photometric Reconstruction Using a Depth Camera. In: *Proceedings of the IEEE Conference on Computer Vision and Pattern Recognition*, pp. 2283–2290. Columbus, USA. (2014) [3](#)
 27. Harker, M., O’Leary, P.: Regularized Reconstruction of a Surface from its Measured Gradient Field. *Journal of Mathematical Imaging and Vision* **51**(1), 46–70 (2015) [4](#), [6](#), [8](#), [9](#), [10](#), [18](#), [21](#)
 28. Hayya, J., Armstrong, D., Gressis, N.: A note on the ratio of two normally distributed variables. *Management Science* **21**(11), 1338–1341 (1975) [17](#)
 29. Hoeltgen, L., Setzer, S., Weickert, J.: An Optimal Control Approach to Find Sparse Data for Laplace Interpolation. In: *Proceedings of the 9th International Workshop on Energy Minimization Methods in Computer Vision and Pattern Recognition, Lecture Notes in Computer Science*, vol. 8081, pp. 151–164. Lund, Sweden (2013) [22](#)
 30. Horn, B.K.P., Brooks, M.J.: *The Variational Approach to Shape From Shading*. *Computer Vision, Graphics, and Image Processing* **33**(2), 174–208 (1986) [4](#)
 31. Horowitz, I., Kiryati, N.: Depth from Gradient Fields and Control Points: Bias Correction in Photometric Stereo. *Image and Vision Computing* **22**(9), 681–694 (2004) [3](#)
 32. Ikehata, S., Wipf, D., Matsushita, Y., Aizawa, K.: Photometric Stereo Using Sparse Bayesian Regression for General Diffuse Surfaces. *IEEE Transactions on Pattern Analysis and Machine Intelligence* **36**(9), 1816–1831 (2014) [11](#)
 33. Kadambi, A., Taamazyan, V., Shi, B., Raskar, R.: Polarized 3D: High-Quality Depth Sensing With Polarization Cues. In: *Proceedings of the 15th IEEE International Conference on Computer Vision*, pp. 3370–3378. Santiago, Chili (2015) [3](#)
 34. Kimmel, R., Yavneh, I.: An Algebraic Multigrid Approach for Image Analysis. *SIAM Journal on Scientific Computing* **24**(4), 1218–1231 (2003) [3](#)
 35. Kornprobst, P., Aubert, G.: Image Sequence Analysis via Partial Differential Equations. *Journal of Mathematical Imaging and Vision* **11**(1), 5–26 (1999) [2](#)
 36. Koutis, I., Miller, G.L., Peng, R.: A Nearly-m log n Time Solver for SDD Linear Systems. In: *Proceedings of the IEEE Annual Symposium on Foundations of Computer Science*, pp. 590–598. Palm Springs, USA (2011) [6](#)
 37. Lanza, A., Morigi, S., Sgallari, F.: Convex Image Denoising via Non-convex Regularization with Parameter Selection. *Journal of Mathematical Imaging and Vision* pp. 1–26 (2016). (in press) [2](#), [14](#)
 38. Mumford, D., Shah, J.: Optimal Approximations by Piecewise Smooth Functions and Associated Variational Problems. *Communications in Pure and Applied Mathematics* **42**(5), 577–685 (1989) [2](#), [11](#), [19](#)
 39. Nikolova, M.: Local Strong Homogeneity of a Regularized Estimator. *SIAM Journal on Applied Mathematics* **61**(2), 633–658 (2000) [2](#), [13](#)
 40. Noakes, L., Kozera, R.: Nonlinearities and Noise Reduction in 3-Source Photometric Stereo. *Journal of Mathematical Imaging and Vision* **18**(2), 119–127 (2003) [18](#)
 41. Ochs, P., Brox, T., Pock, T.: ipiasco: Inertial proximal algorithm for strongly convex optimization. *Journal of Mathematical Imaging and Vision* **53**(2), 171–181 (2015) [2](#)
 42. Ochs, P., Chen, Y., Brox, T., Pock, T.: iPiano: Inertial Proximal Algorithm for Nonconvex Optimization. *SIAM Journal on Imaging Sciences* **7**(2), 1388–1419 (2014) [2](#), [14](#)
 43. Or-el, R., Rosman, G., Wetzler, A., Kimmel, R., Bruckstein, A.M.: RGBD-Fusion: Real-Time High Precision Depth Recovery. In: *Proceedings of the IEEE Conference on Computer Vision and Pattern Recognition*, pp. 5407–5416. Boston, USA. (2015) [3](#)
 44. Pérez, P., Gangnet, M., Blake, A.: Poisson image editing. *ACM Transactions on Graphics* **22**(3), 313–318 (2003) [21](#), [22](#)
 45. Perona, P., Malik, J.: Scale-space and Edge Detection using Anisotropic Diffusion. *IEEE Transactions on Pattern Analysis and Machine Intelligence* **12**(7), 629–639 (1990) [2](#), [11](#), [16](#), [17](#)
 46. Peter, P., Hoffmann, S., Nedwed, F., Hoeltgen, L., Weickert, J.: Evaluating the true potential of diffusion-based inpainting in a compression context. *Signal Processing: Image Communication* **46**, 40 – 53 (2016) [21](#), [22](#)
 47. Pock, T., Cremers, D., Bischof, H., Chambolle, A.: An algorithm for minimizing the Mumford-Shah functional. In: *Proceedings of the 12th IEEE International Conference on Computer Vision*, pp. 1133–1140. Kyoto, Japan (2009) [19](#)
 48. Quéau, Y., Durou, J.D.: Edge-Preserving Integration of a Normal Field: Weighted Least Squares, TV and L1 Approaches. In: *Proceedings of the 5th International Conference on Scale Space and Variational Methods in Computer Vision, Lecture Notes in Computer Science*, vol. 9087, pp. 576–588. Lège Cap-Ferret, France (2015) [1](#), [3](#), [11](#), [12](#), [16](#)
 49. Rudin, L.I., Osher, S., Fatemi, E.: Nonlinear total variation based noise removal algorithms. *Physica D: Nonlinear Phenomena* **60**(1-4), 259–268 (1992) [12](#)
 50. Saracchini, R.F.V., Stolfi, J., Leitão, H.C.G., Atkinson, G.A., Smith, M.L.: A Robust Multi-Scale Integration Method to Obtain the Depth From Gradient Maps. *Computer Vision and Image Understanding* **116**(8), 882–895 (2012) [11](#)
 51. Shefi, R., Teboulle, M.: Rate of Convergence Analysis of Decomposition Methods Based on the Proximal Method of Multipliers for Convex Minimization. *SIAM Journal on Optimization* **24**(1), 269–297 (2014) [13](#)
 52. Shi, B., Wu, Z., Mo, Z., Duan, D., Yeung, S.K., Tan, P.: A Benchmark Dataset and Evaluation for Non-Lambertian and Uncalibrated Photometric Stereo. In: *Proceedings of the IEEE Conference on Computer Vision and Pattern Recognition*. Las Vegas, USA (2016) [18](#)
 53. Simchony, T., Chellappa, R., Shao, M.: Direct Analytical Methods for Solving Poisson Equations in Computer Vision Problems. *IEEE Transactions on Pattern Analysis and Machine Intelligence* **12**(5), 435–446 (1990) [6](#), [8](#), [9](#), [10](#), [18](#)
 54. Weickert, J.: *Anisotropic diffusion in image processing*. Teubner Stuttgart (1998) [16](#)
 55. Woodham, R.J.: Photometric Method for Determining Surface Orientation from Multiple Images. *Optical Engineering* **19**(1), 139–144 (1980) [4](#), [16](#), [18](#), [21](#)